

Assessment of Simulated Soil Moisture from WRF Noah, Noah-MP, and CLM Land Surface Schemes for Landslide Hazard Application

Lu Zhuo^{1,2,3}, Qiang Dai^{1,2,4,*}, Dawei Han², Ningsheng Chen⁵, Binru Zhao^{2,6}

¹Key Laboratory of VGE of Ministry of Education, Nanjing Normal University, Nanjing, China

²WEMRC, Department of Civil Engineering, University of Bristol, Bristol, UK

³Department of Civil and Structural Engineering, University of Sheffield, Sheffield, UK

⁴Jiangsu Center for Collaborative Innovation in Geographical Information Resource Development and Application, Nanjing, China

⁵The Institute of Mountain Hazards and Environment (IMHE), China

⁶College of Water Conservancy and Hydropower Engineering, Hohai University, Nanjing, China

*Correspondence: qd_gis@163.com

Abstract

This study assesses the usability of Weather Research and Forecasting (WRF) model simulated soil moisture for landslide monitoring in the Emilia Romagna region, northern Italy during the 10-year period between 2006 and 2015. Particularly three advanced Land Surface Model (LSM) schemes (i.e., Noah, Noah-MP and CLM4) integrated with the WRF are used to provide detailed multi-layer soil moisture information. Through the temporal evaluation with the single-point in-situ soil moisture observations, Noah-MP is the only scheme that is able to simulate the large soil drying phenomenon close to the observations during the dry season, and it also has the highest correlation coefficient and the lowest *RMSE* at most soil layers. It is also demonstrated that a single soil moisture sensor located in plain area has a high correlation with a significant proportion of the study area (even in the mountainous region 141 km away, based on the WRF simulated spatial soil moisture information). The evaluation of the WRF rainfall estimation shows there is no distinct difference among the three LSMs, and their performances are in line with a published study for the central USA. Each simulated soil moisture product from the three LSM schemes is then used to build a landslide prediction model, and within each model, 17 different exceedance probability levels from 1% to 50% are adopted to determine the optimal threshold scenario (in total there are

28 612 scenarios). Slope degree information is also used to separate the study region into different
29 groups. The threshold evaluation performance is based on the landslide forecasting accuracy using
30 45 selected rainfall events between 2014-2015. Contingency tables, statistical indicators, and
31 Receiver Operating Characteristic analysis for different threshold scenarios are explored. The
32 results have shown that, for landslide monitoring, Noah-MP at the surface soil layer with 30%
33 exceedance probability provides the best landslide monitoring performance, with its hitting rate at
34 0.769, and its false alarm rate at 0.289.

35 **Keywords:** Emilia Romagna, Weather Research and Forecasting (WRF) Model, Land Surface
36 Model (LSM), Numerical Weather Prediction (NWP) model, landslide hazards, soil moisture.

37 **1. Introduction**

38 Landslide is a repeated geological hazard during rainfall seasons, which causes massive
39 destructions, loss of lives, and economic damages worldwide (Klose et al., 2014). The accurate
40 predicting and monitoring of the spatiotemporal occurrence of the landslide is the key to prevent/
41 reduce casualties and damages to properties and infrastructures. One of the most widely adopted
42 methods for landslide prediction is based on rainfall threshold, which relies on building the rainfall
43 intensity-duration curve using the information from the past landslide events (Chae et al., 2017).
44 However, such a method in many cases is insufficient for landslide hazard assessment (Posner and
45 Georgakakos, 2015), because in addition to rainfall, initial soil moisture condition is one of the
46 main triggering factors of the events (Glade et al., 2000; Crozier, 1999; Tsai and Chen, 2010; Hawke
47 and McConchie, 2011; Bittelli et al., 2012; Segoni et al., 2018b; Valenzuela et al., 2018; Bogaard
48 and Greco, 2018).

49 For landslide applications, one potential soil moisture estimation method is through satellite
50 remote sensing technologies. Although such technologies have been improved significantly over
51 the past decade, their retrieving accuracy is still largely affected by frozen soil conditions (Zhuo
52 et al., 2015a), and dense vegetation coverages particularly in mountainous regions (Temimi et al.,
53 2010); furthermore, the acquired data only covers the top few centimetres of soil. Although the
54 more recently launched satellites such as Sentinel-1 (1 km, and 3 days resolution) has shown some
55 promising performance of soil moisture estimation (Gao et al., 2017;Paloscia et al., 2013), its
56 availability only covers the recent years (Geudtner et al., 2014). Those disadvantages restrict the
57 full utilisation of satellite soil moisture products for landslide monitoring application as discussed
58 in our previous study (Zhuo et al., 2019). In Zhuo et al. (2019), it is discussed that both the temporal
59 and spatial resolutions of the ESA CCI satellite soil moisture product (Dorigo et al., 2017) is too
60 coarse for landslide applications, and its data are mostly only available after the year 2002.
61 Moreover, the shallow depth soil moisture observation from the satellite hinders the accuracy of
62 landslide predictions. Therefore, other alternative soil moisture estimation methods need to be
63 explored.

64 One emerging area relies on modelling. Some studies have used modelled soil moisture data for
65 landslide applications (Ponziani et al., 2012;Ciabatta et al., 2016;Zhao et al., 2019a;Zhao et al.,
66 2019b). However, to our knowledge, there is a lack of existing study using the state-of-the-art
67 Land Surface Models (LSMs) modelled soil moisture for landslide studies, such as the Noah LSM
68 (Ek et al., 2003) and the Community Land Model (CLM) (Oleson et al., 2010). LSMs describe the
69 interactions between the atmosphere and the land surface by simulating exchanges of momentum,
70 heat and water within the Earth system (Maheu et al., 2018). They are capable of simulating the
71 most important subsurface hydrological processes (e.g., soil moisture) and can be integrated with

72 the advanced Numerical Weather Prediction (NWP) system like WRF (Weather Research and
73 Forecasting) (Skamarock et al., 2008) for comprehensive soil moisture estimations (i.e., through
74 the surface energy balance, the surface layer stability and the water balance equations) (Greve et
75 al., 2013). NWP-based (i.e., with integrated LSM, thereafter) soil moisture estimations have many
76 advantages, for instance their spatial and temporal resolution can be set at different scales
77 depending on the input datasets to fit various application requirements; their coverage is global,
78 and the estimated soil moisture data covers multiple soil layers (from the shallow surface layer to
79 deep root-zones); as well as a number of globally-covered data products can provide the necessary
80 boundary and initial conditions for running the models. Soil moisture estimated through such an
81 approach has been widely recognised and demonstrated in many studies, which cover a broad
82 range of applications from hydrological modelling (Srivastava et al., 2013a;Srivastava et al., 2015),
83 drought studies (Zaitchik et al., 2013), flood investigations (Leung and Qian, 2009), to regional
84 weather prediction (Stéfanon et al., 2014). Therefore, NWP-based soil moisture datasets could
85 provide valuable information for landslide applications. However, to our knowledge, relevant
86 research has never been carried out.

87 The aim of this study hence is to evaluate the usefulness of NWP modelled soil moisture for
88 landslide monitoring. Here the advanced WRF model (version 3.8) is adopted, because it offers
89 numerous physics options such as micro-physics, surface physics, atmospheric radiation physics,
90 and planetary boundary layer physics (Srivastava et al., 2015), and can integrate with a number of
91 LSM schemes, each varying in physical parameterisation complexities. So far there is limited
92 literature in comparing the soil moisture accuracy of different LSMs options in the WRF model.
93 Therefore, in this study, we select three of the WRF's most advanced LSM schemes (i.e., Noah,
94 Noah-Multiparameterization (Noah-MP), and CLM4) to compare their soil moisture performance

95 for landslide hazard assessment. Furthermore, since all the three schemes can provide multi-layer
96 soil moisture information, it is useful to include all those simulations for the comparison so that
97 the optimal depth of soil moisture could be determined for the landslide monitoring application.
98 In order to compare with the performance of our previous study on using the satellite soil moisture
99 data (Zhuo et al., 2019), the same study area called Emilia Romagna is used here. The study period
100 covers 10 years from 2006 to 2015 to include a long-term record of landslide events. In addition,
101 because slope angle is one of the major factors controlling the stability of the slope, it is hence
102 used in this study to divide the study area into several slope groups, so that a more accurate
103 landslide prediction model could be built.

104 The description of the study area and the used datasets are included in Section 2. Methodologies
105 regarding the WRF model, the related LSM schemes and the adopted landslide threshold
106 evaluation approach are provided in Section 3. Section 4 shows the WRF soil moisture evaluation
107 results against the in-situ observations, and the WRF rainfall evaluations over the whole study area.
108 Section 5 covers the comparison results of the WRF modelled soil moisture products for landslide
109 applications. The discussions and conclusions of the study are included in Section 6 and 7,
110 respectively.

111 **2. Study Area and Datasets**

112 **2.1 Study Area**

113 The study area is in the Emilia Romagna Region, northern Italy (Figure 1). Its population density
114 is high. The region has high mountainous areas in the S-SW, and wide plain areas towards NE,
115 with a large elevation difference (i.e., 0 m to 2125 m) across 50 km distance from the north to the
116 south (Rossi et al., 2010). The region has a mild Mediterranean climate with distinct wet and dry

117 seasons (i.e., dry season between May and October, and wet season between November and April).
118 The study area tends to be affected by landslide events easily, with approximately one-fifth of the
119 mountainous zone covered by active or dormant landslide deposits (Bertolini et al., 2005). Rainfall
120 is by far the primary triggering factor of landslides in the region, followed by snow melting:
121 shallow landslides are mainly triggered by short but exceptionally intense rainfall, and long and
122 moderate rainfall events over saturated conditions, while deep-seated landslides have a more
123 complex response to rainfall and are mainly caused by moderate but exceptionally prolonged (even
124 up to 6 months) periods of rainfalls (Segoni et al., 2015). Due to the abundant data available in the
125 region, several studies on regional scale landslide prediction and early warning have been
126 published (Berti et al., 2012; Martelloni et al., 2012; Lagomarsino et al., 2015; Segoni et al.,
127 2018b; Segoni et al., 2018a; Lagomarsino et al., 2013). Interested readers can refer to those studies
128 for more information.

129 **2.2 Selection of The Landslide Events**

130 The landslides catalog is collected from the Emilia Romagna Geological Survey (Berti et al., 2012).
131 The information included in the catalog are: location, date of occurrence, the uncertainty of date,
132 landslide characteristics (dimensions, type, and material), triggering factors, damages, casualties,
133 and references. Unfortunately, many pieces of the information are missing from the records in
134 many cases. In order to organise the data in a more systematic way so that only the relevant events
135 are retained, a two-step event selection procedure is initially carried out based on: 1) rainfall-
136 induced only; and 2) high spatial-temporal accuracy (exact date and coordinates). Finally, a
137 revision of the information about the type of slope instabilities such as landslide/debris
138 flow/rockfall and the characteristics of the affected slope (natural or artificial) is also carried out
139 over the selected records (Valenzuela et al., 2018). The catalog period used in this study covers

140 between 2006 and 2015, which is in accordance with the WRF model run. After filtering the data
141 records, only one-fifth of them (i.e., 157 events) is retained. The retained events are shown as
142 single circles in Figure 2, with slope information (calculated through the Digital Elevation Model
143 (DEM) data) also presented in the background. It can be seen the spatial distribution of the
144 occurred landslide events is very heterogeneous, with nearly all of them occurred in the hilly
145 regions.

146 **2.3 Datasets**

147 There is a total of 19 soil moisture stations available within the study area, however, based on our
148 collected data, only one of them at the San Pietro Capofiume (latitude 44° 39' 13.59", longitude
149 11° 37' 21.6") provides long-term valid soil moisture retrievals (i.e., 2006 to 2017). We have
150 checked the data from all the rest of the stations, they are either absent (or have very big data gaps)
151 or do not cover the research period at all. Therefore, only the San Pietro Capofiume station is used
152 for the WRF soil moisture temporal evaluation. The soil moisture is measured from 10 cm to 180
153 cm deep in the soil at 5 depths, by the Time Domain Reflectometry (TDR) instrument. Data are
154 recorded in the unit of volumetric water content (m^3/m^3) and at daily timestep (Pistocchi et al.,
155 2008). The data used in this study is between 2006 and 2015. Rainfall data over the whole study
156 area is collected from over 200 tipping-bucket rain gauges, which are used to assess the quality of
157 the WRF model's rainfall estimations in the study area, as well as for rainfall events selection
158 during the Year 2014 and 2015.

159 To drive a NWP model like WRF for soil moisture simulations, several globally-coved data
160 products can be chosen for extracting the boundary and initial conditions information, for instance,
161 the European Centre for Medium-Range Weather Forecasts (ECMWF) reanalysis (ERA-Interim)
162 and the National Centre for Environmental Prediction (NCEP) reanalysis are two of the most

163 commonly used data products. It has been found by (Srivastava et al., 2013b) that the ERA-Interim
164 datasets can provide better boundary conditions than the NCEP datasets for WRF hydro-
165 meteorological predictions in Europe, which is therefore adopted in this study to drive the WRF
166 model. The spatial resolution of the ERA-Interim is approximately 80 km. The data is available
167 from 1979 to present, containing 6-hourly gridded estimates of three-dimensional meteorological
168 variables, and 3-hourly estimates of a large number of surface parameters and other two-
169 dimensional fields. A comprehensive description of the ERA-Interim datasets can be found in (Dee
170 et al., 2011)

171 The Shuttle Radar Topography Mission (SRTM) 3 Arc-Second Global (~ 90m) DEM datasets are
172 downloaded and used as the basis for the slope degree calculations. SRTM DEM data has been
173 widely used for elevation-related studies worldwide due to its high quality, near-global coverage,
174 and free availability (Berry et al., 2007).

175 **3. Methodologies**

176 **3.1 WRF Model and The Three Land Surface Model Schemes**

177 The WRF model is a next-generation, non-hydrostatic mesoscale NWP system designed for both
178 atmospheric research and operational forecasting applications (Skamarock et al., 2005). The model
179 is powerful enough in modelling a broad range of meteorological applications varying from tens
180 of metres to thousands of kilometres (NCAR, 2018). It has two dynamical solvers: the ARW
181 (Advanced Research WRF) core and the NMM (Nonhydrostatic Mesoscale Model) core. The
182 former has more complex dynamic and physics settings than the latter which only has limited
183 setting choices. Hence in this study WRF with ARW dynamic core (version 3.8) is used to perform
184 all the soil moisture simulations.

185 The main task of LSM within the WRF is to integrate information generated through the surface
186 layer scheme, the radiative forcing from the radiation scheme, the precipitation forcing from the
187 microphysics and convective schemes, and the land surface conditions to simulate the water and
188 energy fluxes (Ek et al., 2003). WRF provides several LSM options, among which three of them
189 are selected in this study as mentioned in the introduction: Noah, Noah-MP, and CLM4. Table 1
190 gives a simple comparison of the three models. The detailed description of the models is written
191 below in the order of increasing complexity in regards of the way they deal with thermal and
192 moisture fluxes in various layers of soil, and their vegetation, root and canopy effects
193 (Skamarock et al., 2008).

194 **3.1.1 Noah**

195 Noah is the most basic amongst the three selected LSMs. It is one of the ‘second generation’ LSMs
196 that relies on both soil and vegetation processes for water budgets and surface energy closures
197 (Wei et al., 2010). The model is capable of modelling soil and land surface temperature, snow
198 water equivalent, as well as the general water and energy fluxes. The model includes four soil
199 layers that reach a total depth of 2 m in which soil moisture is calculated. Its bulk layer of canopy
200 -snow-soil (i.e., lack the abilities in simulating photosynthetically active radiation (PAR),
201 vegetation temperature, correlated energy, and water, heat and carbon fluxes), ‘leaky’ bottom (i.e.,
202 drained water is removed immediately from the bottom of the soil column which can result in
203 much fewer memories of antecedent weather and climate fluctuations) and simple snow melt-thaw
204 dynamics are seen as the model’s demerits (Wharton et al., 2013). Noah calculates the soil moisture
205 from the diffusive form of Richard’s equation for each of the soil layer (Greve et al., 2013), and
206 the evapotranspiration from the Ball-Berry equation (considering both the water flow mechanism

207 within soil column and vegetation, as well as the physiology of photosynthesis (Wharton et al.,
208 2013)).

209 **3.1.2 Noah-MP**

210 Noah-MP (Niu et al., 2011) is an improved version of the Noah LSM, in the aspect of better
211 representations of terrestrial biophysical and hydrological processes. Major physical mechanism
212 improvements directly relevant to soil water simulations include: 1) introducing a more permeable
213 frozen soil by separating permeable and impermeable fractions (Cai, 2015), 2) adding an
214 unconfined aquifer immediately beneath the bottom of the soil column to allow the exchange of
215 water between them (Liang et al., 2003), and 3) the adoption of a TOPMODEL (TOPography
216 based hydrological MODEL)-based runoff scheme (Niu et al., 2005) and a simple SIMGM
217 groundwater model (Niu et al., 2007) which are both important in improving the modelling of soil
218 hydrology. Noah-MP is unique compared with the other LSMs, as it is capable of generating
219 thousands of parameterisation schemes through the different combinations of “dynamic leaf,
220 canopy stomatal resistance, runoff and groundwater, a soil moisture factor controlling stomatal
221 resistance (the β factor), and six other processes” (Cai, 2015). The scheme option used in the study
222 are: Ball-Berry scheme for canopy stomatal resistance, Monin-Obukhov scheme for surface layer
223 drag coefficient calculation, the Noah based soil moisture factor for stomatal resistance, the
224 TOPMODEL runoff with the SIMGM groundwater, the linear effect scheme for soil permeability,
225 the two-stream applied to vegetated fraction scheme for radiative transfer, the CLASS (Canadian
226 Land Surface Scheme) scheme for ground surface albedo option, and the Jordan (Jordan, 1991)
227 scheme for partitioning precipitation between snow and rain.

228 **3.1.3. CLM4**

229 CLM4 is developed by the National Center for Atmospheric Research (NCAR) to serve as the land
230 component of its Community Earth System Model (formerly known as the Community Climate
231 System Model) (Lawrence et al., 2012). It is a ‘third generation’ model that incorporates the
232 interactions of both nitrogen and carbon in the calculations of water and energy fluxes. Compared
233 with its previous versions, CLM4 (Oleson et al., 2008) has multiple enhancements relevant to soil
234 moisture computing. For instance, the model’s soil moisture is estimated by adopting an improved
235 one-dimensional Richards equation (Zeng and Decker, 2009); the new version allows the dynamic
236 interchanges of soil water and groundwater through an improved definition of the soil column’s
237 lower boundary condition that is similar to the Noah-MP’s (Niu et al., 2007). Furthermore, the
238 thermal and hydrologic properties of organic soil are included for the modelling which is based on
239 the method developed in (Lawrence and Slater, 2008). The total ground column is extended to 42
240 m depth, consisting 10 soil layers unevenly spaced between the top layer (0.0–1.8 cm) and the
241 bottom layers (229.6–380.2 cm), and 5 bedrock layers to the bottom of the ground column
242 (Lawrence et al., 2011). Soil moisture is estimated for each soil layer.

243 **3.2 WRF Model Parameterization**

244 The WRF model is centred over the Emilia Romagna Region with three nested domains (D1, D2,
245 D3 with the horizontal grid sizes of 45 km, 15 km, and 5 km, respectively), of which the innermost
246 domain (D3, with 88 x 52 grids (west-east and south-north, respectively)) is used in this study. A
247 two-way nesting scheme is adopted allowing information from the child domain to be fed back to
248 the parent domain. With atmospheric forcing, static inputs (e.g., soil and vegetation types), and
249 parameters, the WRF model needs to be spin-up to reach its equilibrium state before it can be used
250 (Cai et al., 2014;Cai, 2015). In this study, WRF is spin-up by running through the whole year of

251 2005. After the spin-up, the WRF model for each of the selected LSM scheme is executed in daily
252 timestep from January 1, 2006, to December 31, 2015, using the ERA-Interim datasets.

253 The microphysics scheme plays a vital role in simulating accurate rainfall information which in
254 turn is important for modelling the accurate soil moisture variations. WRF V3.8 is supporting 23
255 microphysics options range from simple to more sophisticated mixed-phase physical options. In
256 this study, the WRF Single-Moment 6-class scheme is adopted which considers ice, snow and
257 graupel processes and is suitable for high-resolution applications (Zaidi and Gisen, 2018). The
258 physical options used in the WRF setup are Dudhia shortwave radiation (Dudhia, 1989) and Rapid
259 Radiative Transfer Model (RRTM) longwave radiation (Mlawer et al., 1997). Cumulus
260 parameterization is based on the Kain-Fritsch scheme (Kain, 2004) which is capable of
261 representing sub-grid scale features of the updraft and rain processes, and such a capability is
262 beneficial for real-time modelling (Gilliland and Rowe, 2007). The surface layer parameterization
263 is based on the Revised fifth-generation Pennsylvania State University–National Center for
264 Atmospheric Research Mesoscale Model (MM5) Monin-Obukhov scheme (Jiménez et al., 2012).
265 The Yonsei University scheme (Hong et al., 2006) is selected to calculate the planetary boundary
266 layer. The parameterization schemes used in the WRF modelling are shown in Table 2. The
267 datasets for land use and soil texture are available in the pre-processing package of WRF. In this
268 study, the land use categorisation is interpolated from the MODIS 21-category data classified by
269 the International Geosphere Biosphere Programme (IGBP). The soil texture data are based on the
270 Food and Agriculture Organization of the United Nations Global 5-minutes soil database.

271 **3.3 Translation of Observed and Simulated Soil Moisture Data to Common Soil Layers**

272 Since all soil moisture datasets have different soil depths, it is difficult for a direct comparison.
273 The Noah and Noah-MP models include four soil layers, centred at 5, 25, 70, and 150 cm,

274 respectively. Whereas CLM4 model has 10 soil layers, centered at 0.9, 3.2, 6.85, 12.85, 22.8, 39.2,
275 66.2, 110.65, 183.95, 304.9 cm, respectively. Moreover, the in-situ sensor measures soil moisture
276 centred at 10, 25, 70, 135, and 180 cm. In order to make the datasets comparable at consistent soil
277 depths, the simple linear interpolation approach described in (Zhuo et al., 2015b) is applied in this
278 study, and a benchmark of the soil layer centred at 10, 25, 70 and 150 cm is adopted.

279 **3.4 Soil Moisture Thresholds Build Up and Evaluations**

280 To build and evaluate the soil moisture thresholds for landslides forecasting, all datasets have been
281 grouped into two portions: 2006-2013 for the establishment of thresholds, and 2014-2015 for the
282 evaluation. The determination of soil moisture thresholds is based on determining the most suitable
283 soil moisture triggering level for landslides occurrence by trying a range of exceedance
284 probabilities (percentiles). For example, a 10% exceedance probability is calculated by
285 determining the 10% percentile result of the soil moisture datasets that are related to the occurred
286 landslides. The exceedance probability method is commonly utilised in landslide early warning
287 studies for calculating the rainfall-thresholds, which is therefore adopted here to examine its
288 performance for soil moisture threshold calculations.

289 To carry out the threshold evaluation, 45 rainfall events (during 2014-2015) are selected for the
290 purpose. The rainfall events are separated based on at least one-day of dry period (i.e., a period
291 without rainfall). The rainfall data from each rain gauge station is firstly combined using the
292 Thiessen Polygon method, and with visual analysis, the 45 events are then finally selected. The
293 information about the selected rainfall events can be found in Section 5. The threshold evaluation
294 is based on the statistical approach described in (Gariano et al., 2015;Zhuo et al., 2019), where soil
295 moisture threshold can be treated as a binary classifier of the soil moisture conditions that are likely
296 or unlikely to cause landslide events. With this hypothesis, the likelihood of a landslide event can

297 either be *true (T)* or *false (F)*, and the threshold forecasting can either be *positive (P)* or *negative*
298 *(N)*. The combinations of those four conditions can lead to four statistical outcomes (Figure 3a)
299 that are: *true positive (TP)*, *true negative (TN)*, *false positive (FP)*, and *false negative (FN)* (Wilks,
300 2011). Using the four outcomes, two statistical scores can be determined.

301 The Hit Rate (*HR*), which is the rate of the events that are correctly forecasted. Its formula is:

$$302 \quad HR = \frac{TP}{TP+FN} \quad (1)$$

303 in the range of 0 and 1, with the best result as 1.

304 The False Alarm Rate (*FAR*), which is the rate of false alarms when the event did not occur. Its
305 formula is:

$$306 \quad FAR = \frac{FP}{FP+TN} \quad (2)$$

307 in the range of 0 and 1, with the best result as 0.

308 For any soil moisture product, each threshold calculated is adopted to determine *T*, *F*, *P*, and *N*,
309 respectively. Those values are finally integrated to find the overall scores of *TP*, *FN*, *FP*, *TN*, *HR*,
310 and *FAR*. The threshold performance is then judged via the Receiver Operating Characteristic
311 (ROC) analysis (Hosmer and Lemeshow, 1989;Fawcett, 2006). As shown in Figure 3b, ROC curve
312 is based on *HR* against *FAR*, and each point in the curve represents a threshold scenario (i.e.,
313 selected exceedance probabilities). The optimal result (the red point) can only be realised when
314 the *HR* reaches 1 and the *FAR* reduces to 0. The closer the point to the red point, the better the
315 forecasting result is. To analyse and compare the forecasting performance numerically, the
316 Euclidean distances (*d*) for each scenario to the optimal point are computed.

317 **4. WRF Model Evaluations**

318 In this study, the evaluation is based on the daily mean soil moisture. The reason for not using the
319 antecedent soil moisture condition plus rainfall data on the day is because the purpose of this study
320 is to explore the relationship between different WRF simulated soil moisture and landslides solely.

321 In general, soil moisture is a predisposing factor for slope instability, while rainfall is the triggering
322 factor. The same rainfall may trigger or not a landslide depending on the soil moisture content at
323 the time of the rainfall event. The mean soil moisture on the day of the landslide implicitly account
324 for both the initial soil moisture and the effective rainfall absorbed by the ground, and can be a
325 robust indicator of the hydrological condition of the slope.

326 **4.1 Soil Moisture Temporal Comparisons**

327 Although there is only one soil moisture sensor that provides long-term soil moisture data in the
328 study region, it is still useful to compare it with the WRF estimated soil moisture. In this study, we
329 carry out a temporal comparison between all the three WRF soil moisture products with the in-situ
330 observations (at a single soil moisture measuring point in the plain area). The comparison is
331 implemented over the period from 2006 to 2015, and the WRF grid closest to the in-situ sensor
332 location is chosen. Figure 4 shows the comparison results at the four soil depths. The statistical
333 performance (correlation coefficient r and Root Mean Square Error $RMSE$) of the three LSM
334 schemes are summarised in Table 3. Based on the statistical results, Noah-MP surpasses other
335 schemes at most soil layers, except for Layer 2 where CLM4 shows stronger correlation and Layer
336 4 where Noah gives smaller $RMSE$ error. For Noah-MP, the best correlation is observed at the
337 surface layer (0.809), followed by the third (0.738), second (0.683) and fourth (0.498) layers; and
338 based on $RMSE$, the best performance is again observed at the surface layer and followed by the
339 second, third and fourth layers in sequence (as 0.060, 0.070, 0.088, and 0.092 m^3/m^3 , respectively).
340 From the temporal plots, it can be seen at all four soil layers, all three LSM schemes can produce
341 the soil moisture's seasonal cycle with most upward and downward trends successfully represented.
342 However, both the Noah and the CLM4 overestimate the variability at the upper two soil layers
343 during almost the whole study period, and the situation is the worst for the Noah. Comparatively,

344 the Noah-MP can better capture the wet soil moisture conditions especially at the surface layer;
345 and it is the only model of the three that is able to simulate the large soil drying phenomenon close
346 to the observations during the dry season, except for some extremely dry days. Towards 70 cm
347 depth, although Noah-MP is still able to capture most of the soil moisture variabilities during the
348 drying period, it significantly underestimates soil moisture values for most wet days. Similar
349 underestimation results can be observed for CLM4 and Noah during the wet season at 70 cm;
350 furthermore, both schemes are again not capable of reproducing the extremely drying phenomenon
351 and overestimate soil moisture for most of the dry season days. It is surprising to see that at the
352 deep soil layer (150 cm), all soil moisture products are underestimated, in particular, the outputs
353 from the CLM4 and the Noah-MP only show small fluctuations. However, the soil moisture
354 measurements from the in-situ sensor also get our attention as they show strange fluctuations with
355 numerous sudden drops and rise situations observed. The strange phenomenon is not expected at
356 such a deep soil layer (although groundwater capillary forces can increase the soil moisture, its
357 rate is normally very slow). One possible reason we suspect is due to sensor failure in the deep
358 zone. Therefore, the assessment result for the deep soil layer should be considered unreliable.
359 Overall for the Noah-MP, in addition to producing the highest correlation coefficient and the
360 lowest *RMSE*, its simulated soil moisture variations are the closest to the observations. The better
361 performance of the Noah-MP over the other two models agrees with the results found in (Cai et
362 al., 2014) (note: the paper uses standalone models, which are not coupled with WRF). Also, it has
363 been discussed in (Yang et al., 2011), the Noah MP presents a clear improvement over the Noah
364 in simulating soil moisture globally. However, it is noted the evaluation results are only based on
365 one soil moisture sensor located at the plain part of the study area.

366 **4.2 Rainfall Evaluations**

367 Since soil moisture is related to rainfall, it is useful to carry out the evaluations of WRF rainfall
368 estimations against the observations in the study area. The spatial plot of R for the three LSMs is
369 shown in Figure 5. It can be seen the performance of the three models are very close to each other,
370 with only small differences over the whole study region. In general, the performance is the best in
371 the Southeast region, with R reaches above 0.70. The poorest performance is observed in the
372 Northeast region and some parts of the mountain zone. Based on the spatial distribution of R , there
373 is no clear correlation between the WRF rainfall performance and the topography of the region.
374 The boxplot for the R performance is illustrated in Figure 6a. It can be seen again the performances
375 of the three models are very similar. Generally, R ranges between around 0.10 and 0.80, and with
376 the majority of the region performs around 0.40. $RMSE$ performance is also calculated. Similar to
377 the results of R , it has been found the $RMSE$ spatial distributions are very similar among the three
378 models. Therefore, the $RMSE$ spatial distribution map is not included in this paper. The boxplot of
379 the $RMSE$ is shown in Figure 6b. Generally, the $RMSE$ ranges between around 4 mm and 12 mm,
380 with some outliers between around 12 mm and 20 mm. Majority of the region performs at around
381 7 mm $RMSE$. The statistical calculations are summarised in Table 4. Based on the results of R and
382 $RMSE$, the WRF rainfall estimation performance in Emilia is similar to the one found in central
383 USA (Van Den Broeke et al., 2018).

384 **5. The Assessment of WRF Soil Moisture Threshold for Landslide Monitoring**

385 As introduced at the beginning of the paper, previous works (as discussed in the introduction
386 section) have demonstrated that in complex geomorphologic settings (e.g., in Emilia Romagna), a
387 rainfall threshold approach is too simple and more hydrologically driven approaches need to be
388 established. This section is to assess if the spatial distribution of soil moisture can provide useful
389 information for landslide monitoring at the regional scale. Particularly, all three soil moisture

390 products simulated through the WRF model are used to derive threshold models, and the
391 corresponding landslide prediction performances are then compared statistically. Here the
392 threshold is defined as the crucial soil moisture condition above which landslides are likely to
393 happen.

394 Among different factors for controlling the stability of slope, the slope angle is one of the most
395 critical ones. From the slope angle map in Figure 2, it can be seen the region has a clear spatial
396 pattern of high and low slope areas, with the majority of the high-slope areas (can be as steep as
397 around 40 degrees) located in the mountainous Southern part and the river valleys. Based on the
398 analysed events data, the landslides happened during the study period are mainly located in the
399 high-slope region, with a particularly high concentration around the central Southern part. The
400 spatial distribution of the landslide events is also in line with the overall geological characteristics
401 of the region, i.e., the Southern part mainly constitutes outcrop of sandstone rocks that make up
402 the steep slopes and are covered by a thin layer of permeable sandy soil, which are highly unstable.
403 Therefore, instead of only using one soil moisture threshold for the whole study area, it is useful
404 to divide the region into several slope groups so that within each group a threshold model is built.
405 To derive soil moisture threshold individually under different slope conditions, all data has been
406 divided into three groups based on the slope angle (0.4-1.86°; 1.87-9.61°; 9.52-40.43°; since no
407 landslide events are recorded under the 0-0.39° group, the group is not considered here), as results,
408 all groups have equal coverage areas. There are different ways to group the slopes. In this study,
409 in order to have equal coverage areas, we have identified these class-break values.

410 In order to find the optimal threshold so that there are least missing alarms (i.e., threshold is
411 overestimated) and false alarms (i.e., threshold is underestimated), we test out 17 different
412 exceedance probabilities from 1% to 50%. For each LSM scheme, the total number of threshold

413 models is 204, which is the resultant of different combinations of slope groups, soil layers, and
414 exceedance probability conditions. The calculated thresholds for all LSM schemes under three
415 slope groups are plotted in Figure 7. Overall there is a clear trend between the slope angle and the
416 soil moisture threshold, that is with threshold becoming smaller for steeper areas. The correlation
417 is more evident at the upper three soil layers (i.e., the top 1 m depth of soil), with only a few
418 exceptions for Noah and CLM4 at the 1% and the 2% exceedance probabilities. At the deep soil
419 layer centred at 150 cm, the soil moisture threshold difference between Slope Group (S.G.) 2 and
420 3 becomes very small for all the three LSM schemes. This could be partially because at the deep
421 soil layer, the change of soil moisture is much smaller than at the surface layer, therefore the soil
422 moisture values for S.G. 2 and 3 could be too similar to differentiate. However, for milder slopes
423 (S.G. 1), the higher soil moisture triggering level always applies even down to the deepest soil
424 layer for all the three LSM schemes. In this study, the results show that wetter soil can trigger
425 landslides easier in milder slopes than in steeper slopes.

426 All the threshold models are then evaluated under the 45 selected rainfall events (Table 5) using
427 the ROC analysis. Each threshold determined for each of the slope class during the calibration is
428 used for the evaluation. The period of the selected rainfall events is between 1 day and 18 days,
429 and the average rainfall intensity ranges from 5.05 mm/day to 24.69 mm/day. The resultant
430 Euclidean distances (d) between each scenario of exceedance probability and the optimal point for
431 ROC analysis are listed in Table 6 for all three WRF LSM schemes at the tested exceedance
432 probabilities. The best performance (i.e., lowest d) in each column (i.e., each soil layer of an LSM
433 scheme) is highlighted. In addition, the d results are also plotted in Figure 8 to give a better view
434 of the overall trend amongst different soil layers and LSM schemes. From the figure, for all three
435 LSM schemes at all four soil layers, there is an overall downward and then stabilised trend. Overall

436 for Noah, the simulated surface layer soil moisture provides better landslide monitoring
437 performance than the rest of the soil layers from 1% to 35% exceedance probabilities; and the
438 scheme's worst performance is observed at the third soil layer centred at 70 cm. The values of d
439 for Noah's second and fourth layer are quite close to each other. For Noah-MP, the simulated
440 surface layer soil moisture gives the best performance amongst all four soil layers for most cases
441 between the 1% and 35% exceedance probability range; and the scheme's worst performance is
442 observed at the fourth layer. Unlike Noah, all four soil layers from the Noah-MP scheme provide
443 distinct performance amongst them (i.e., larger d difference). For CLM4, the performance for the
444 surface layer is quite similar to the second layer's, and the differences between the four layers are
445 small. From the Table 6, it can be seen for Noah the most suitable exceedance probabilities (i.e.,
446 the highlighted numbers) range between 35% to 50%; for Noah-MP they are between 30% and
447 50%, and for CLM4 it stays at 40% for all four soil layers. For both Noah and Noah-MP, the best
448 performance is observed at the surface layer ($d = 0.392$ and $d = 0.369$, respectively). For CLM4,
449 the best performances show no distinct pattern amongst soil layers (i.e., with the best performance
450 found at the soil Layer 3, followed by Layer 2, 1, and 4). Of all the LSM schemes and soil layers,
451 the best performance is found for Noah-MP at the surface layer with 30% exceedance probability
452 ($d=0.369$). Based on the d results, WRF modelled soil moisture provides better landslide prediction
453 performance than the satellite ESA-CCI soil moisture products as shown in our previous study
454 ((Zhuo et al., 2019), i.e., $d = 0.51$). The ROC curve for the Noah-MP scheme at the surface layer
455 is shown in Figure 9. In the curve, each point represents a scenario with a selected exceedance
456 probability level. It is clear with various exceedance probabilities, FAR can be decreased without
457 sacrificing the HR score (e.g., 4% to 10% exceedance probabilities). At the optimal point at the

458 30% exceedance probability, the best results for *HR* and *FAR* are observed as 0.769 and 0.289,
459 respectively.

460 **6. Discussions**

461 In this study, the best landslide prediction performance for Noah and Noah-MP follows a regular
462 trend, that is the deeper the soil layer, the poorer the landslide monitoring performance. There are
463 several potential reasons for such an outcome. First, the simulated soil moisture accuracy at the
464 shallower layers are better than the deeper zones. Second, although the wetness conditions at the
465 sliding surface are important, the soil moisture above it is also important (i.e., the loading should
466 be heavier with more water in the upper soil layer). Third, the landslides occurred in the region are
467 mainly in the top shallow soil layer. Fourth, the WRF modelled soil moisture is not accurate
468 enough in assessing the landslide events in the study region. In order to find out the extract reasons,
469 comprehensive studies with more detailed landslide events datasets are needed in future studies.

470 For the WRF soil moisture evaluation, clearly the evaluation work based on a single soil moisture
471 sensor located in plain area is not sufficient to derive conclusions about the model's performance
472 over the whole study region. Therefore, the results are preliminary here. However, in this study,
473 by introducing the WRF spatial soil moisture information into the landslide prediction model, the
474 performance indeed has been improved in comparison with our previous study using the satellite
475 remote sensing soil moisture data (Zhuo et. al 2019). A similar concept has been carried out by
476 Segoni et al., (2018b), who implemented the soil moisture information simulated from a
477 hydrological model into a regional landslide early warning system with clear improvements in
478 false/ missing alarm performance. Although the results shown in this study is preliminary and
479 confined by the study area, the improved landslide prediction performance is already obtained.

480 Therefore, it is hoped with more densely soil moisture network data available globally and further
481 refinements of the method, the results could be improved further.

482 In addition, ideally, it will be useful if there is a dense soil moisture sensing network covering the
483 whole study area. In reality, that's not practical, so we have to rely on the spatial soil moisture
484 information by other means. So far, the soil moisture data with the best spatial and temporal
485 resolution is from the WRF model. A question is about how representative of a single soil moisture
486 sensor is for the whole study area. We have carried out the correlation study of a single sensor with
487 the whole study region (using the Noah-MP top-layer soil moisture data). As seen in Figure 10a,
488 the study region is divided into 44 equal-spacing grids (30 km apart), with the grid centres marked
489 as black crosses. The initial assumption is that the soil moisture sensor can only represent its
490 adjacent area, but the result was a surprise (Figure 10b). Based on the outcome, a single point
491 sensor can represent a significant proportion of the region. Admittedly, there are some areas where
492 the correlations are poor, in particular, the Grid 27, which has been compared with its surrounding
493 four grids as shown in Figure 11. It can be seen the soil moisture variation at Grid 27 is totally
494 different in comparison with the four surrounding grids'. The unique soil moisture variation pattern
495 observed in Grid 27 may be caused by different land use and soil type in that area, but clearly
496 further studies are needed to find out the exact reasons. The aforementioned work has prompt us
497 to a future study on the optimal soil moisture sensor network design for landside applications.
498 Although there are numerous studies on the rain gauge network design by the research community,
499 the soil moisture sensor network design has been largely ignored by the community. Hence, this
500 study has paved a foundation for such research.

501 For the WRF rainfall evaluations, the results are not good. Rainfall is one of the main drivers of
502 soil moisture change, and it is logical to think soil moisture and rainfall are highly linked, However,

503 since rainfall temporal variation is of high frequency data while soil moisture is of low frequency,
504 they behave differently. The results illustrate that for landslide study, it is better to use the WRF
505 soil moisture data than its rainfall data. Clearly more studies are needed to confirm this assumption.
506 Here, WRF is modelled based on the ERA-Interim datasets, however, it has been found in Albergel
507 et al. (2018), the performance of using the ERA5 has surpassed the ERA-Interim. Therefore, the
508 ERA5 datasets will be tested in our future studies. Model-based soil moisture estimations could be
509 affected by error accumulation issues, especially in the real-time forecasting mode. A potential
510 solution is to use data assimilation methodologies to correct such errors by assimilating soil
511 moisture information from other data sources. Since in-situ soil moisture sensors are only sparsely
512 available in limited regions, soil moisture measured via satellite remote sensing technologies could
513 provide useful alternatives. Another issue is with the landslide record data, since most of them are
514 based on human experiences (e.g., through newspapers, and victims), a lot of incidences could be
515 unreported. Therefore, the conclusion made here could be biased. Other ways of expanding the
516 current landslide catalog can depend on automatic landslide detection methods based on remote
517 sensing images (Nichol and Wong, 2005;Chen et al., 2018), internet news (as all landslides with a
518 relevant impact on society will be reported on internet news), and automatic web data mining
519 methods (Battistini et al., 2013;Goswami et al., 2018).

520 **7. Conclusions**

521 In this study, the usability of WRF modelled soil moisture for landslide monitoring has been
522 evaluated in the Emilia Romagna region based on the research duration between 2006 and 2015.
523 Specifically, the four-layer soil moisture information simulated through the WRF's three most
524 advanced LSM schemes (i.e., Noah, Noah-MP and CLM4) is compared for the purpose. Through
525 the temporal comparison with the in-situ soil moisture observations, it has been found that all three

526 LSM schemes at all four soil layers can produce the general soil moisture's seasonal cycle.
527 However, only Noah-MP is able to simulate the large soil drying phenomenon close to the
528 observations during the drying season, and it also has the highest correlation coefficient and the
529 lowest *RMSE* at most soil layers amongst the three LSM schemes. However, it should be noted,
530 the soil moisture evaluation is only based on a single point-based soil moisture sensor that is
531 available in the plain region of the study area. Therefore, the WRF soil moisture performance over
532 the whole study region, in particular, at the mountainous zone cannot be evaluated in this study.
533 Since soil moisture is related to rainfall, we have carried out the WRF rainfall assessments, based
534 on the comparison with the dense rainfall network in the region. The results have shown that there
535 is no distinct difference between the three LSM schemes. The WRF rainfall performance is found
536 to be similar to a study carried out over the central USA (Van Den Broeke et al., 2018). A landslide
537 prediction model based on soil moisture and slope angle condition is built up. 17 various
538 exceedance probably levels between 1% and 50% are adopted to find the optimal threshold
539 scenario. Through the ROC analysis of 612 threshold models, the best performance is obtained by
540 the Noah-MP at the surface soil layer with 30% exceedance probability.

541 In summary, this study provides an overview of the soil moisture performance of three WRF LSM
542 schemes for landslide hazard assessment. Based on the results, we demonstrate that the surface
543 soil moisture (centred at 10 cm) simulated through the Noah-MP LSM scheme is useful in
544 predicting landslide occurrences in the Emilia Romagna region. With the hitting rate of 0.769 and
545 the false alarm rate of 0.289 obtained in this study, such soil moisture information has the potential
546 in working with rainfall data to provide landslide predictions. The further study on investigating
547 the soil moisture representation of a single soil moisture sensor over a large region has also been
548 carried out. The results demonstrate that although there is a significant elevation difference in the

549 region, a single soil moisture sensor has a high correlation with a significant proportion of the
550 study area. Although there are still a small proportion of areas where the correlation is poor, this
551 has prompt us to carry out a future study on the optimal design of soil moisture sensor network for
552 landslide study.

553 One must bear in mind that although the results demonstrated in this study are only valid for the
554 selected region, the methodology could be generalised to derive site-specific calibrations in other
555 sites using the proposed approach. In order to make a general conclusion, more researches are
556 needed using the methodology described in this paper. Particularly, a considerable number of
557 catchments with a broad spectrum of climate and environmental conditions and dense soil moisture
558 sensor network will need to be investigated.

559 **Data availability**

560 The in-situ soil moisture and rainfall data can be downloaded from
561 <http://www.smr.arpa.emr.it/dext3r/>; the Landslide inventory data is kindly provided by Dr Matteo
562 Berti, University of Bologna.

563 **Author contribution**

564 Lu Zhuo carried out the modelling of WRF, evaluated its soil moisture performance in landslide
565 prediction, and prepared the manuscript with contributions from all co-authors. Qiang Dai and
566 Binru Zhao processed the in-situ rain gauge datasets (>200 rain gauge stations). Dawei Han and
567 Ningsheng Chen provided guidance on the paper's main research direction and are the funding
568 holders of this project in the UK and China, respectively.

569 **Competing interests**

570 The authors declare that they have no conflict of interest.

571 **Acknowledgement**

572 This study is supported by National Natural Science Foundation of China (No: 41871299);
573 Resilient Economy and Society by Integrated SysTems modelling (RESIST), Newton Fund via
574 Natural Environment Research Council (NERC) and Economic and Social Research Council
575 (ESRC) (NE/N012143/1), and the National Natural Science Foundation of China (No :
576 4151101234).

577 **References**

- 578 Albergel, C., Dutra, E., Munier, S., Calvet, J.-C., Munoz-Sabater, J., Rosnay, P. d., Balsamo, G. J.
579 H., and Sciences, E. S.: ERA-5 and ERA-Interim driven ISBA land surface model simulations:
580 which one performs better?, 22, 3515-3532, 2018.
- 581 Battistini, A., Segoni, S., Manzo, G., Catani, F., and Casagli, N. J. A. G.: Web data mining for
582 automatic inventory of geohazards at national scale, 43, 147-158, 2013.
- 583 Berry, P., Garlick, J., and Smith, R.: Near-global validation of the SRTM DEM using satellite
584 radar altimetry, *Remote Sensing of Environment*, 106, 17-27, 2007.
- 585 Berti, M., Martina, M., Franceschini, S., Pignone, S., Simoni, A., and Pizziolo, M.: Probabilistic
586 rainfall thresholds for landslide occurrence using a Bayesian approach, *Journal of Geophysical*
587 *Research: Earth Surface*, 117, 2012.
- 588 Bertolini, G., Guida, M., and Pizziolo, M. J. L.: Landslides in Emilia-Romagna region (Italy):
589 strategies for hazard assessment and risk management, 2, 302-312, 2005.
- 590 Bittelli, M., Valentino, R., Salvatorelli, F., and Pisa, P. R.: Monitoring soil-water and displacement
591 conditions leading to landslide occurrence in partially saturated clays, *Geomorphology*, 173, 161-
592 173, 2012.

593 Bogaard, T., and Greco, R.: Invited perspectives: Hydrological perspectives on precipitation
594 intensity-duration thresholds for landslide initiation: proposing hydro-meteorological thresholds,
595 *Natural Hazards and Earth System Sciences*, 18, 31-39, 2018.

596 Cai, X., Yang, Z. L., Xia, Y., Huang, M., Wei, H., Leung, L. R., and Ek, M. B.: Assessment of
597 simulated water balance from Noah, Noah- MP, CLM, and VIC over CONUS using the NLDAS
598 test bed, *Journal of Geophysical Research: Atmospheres*, 119, 13,751-713,770, 2014.

599 Cai, X.: Hydrological assessment and biogeochemical advancement of the Noah-MP land surface
600 model, Doctor of Philosophy, Geological Sciences, The University of Texas at Austin, 164 pp.,
601 2015.

602 Chae, B.-G., Park, H.-J., Catani, F., Simoni, A., and Berti, M.: Landslide prediction, monitoring
603 and early warning: a concise review of state-of-the-art, *Geosciences Journal*, 21, 1033-1070, 2017.

604 Chen, F., and Dudhia, J.: Coupling an advanced land surface-hydrology model with the Penn State-
605 NCAR MM5 modeling system. Part I: Model implementation and sensitivity, *Monthly Weather*
606 *Review*, 129, 569-585, 2001.

607 Chen, Z., Zhang, Y., Ouyang, C., Zhang, F., and Ma, J. J. S.: Automated landslides detection for
608 mountain cities using multi-temporal remote sensing imagery, 18, 821, 2018.

609 Ciabatta, L., Camici, S., Brocca, L., Ponziani, F., Stelluti, M., Berni, N., and Moramarco, T. J. J.
610 o. H.: Assessing the impact of climate-change scenarios on landslide occurrence in Umbria Region,
611 *Italy*, 541, 285-295, 2016.

612 Crozier, M. J.: Prediction of rainfall- triggered landslides: A test of the antecedent water status
613 model, *Earth surface processes and landforms*, 24, 825-833, 1999.

614 Dee, D. P., Uppala, S. M., Simmons, A., Berrisford, P., Poli, P., Kobayashi, S., Andrae, U.,
615 Balmaseda, M., Balsamo, G., and Bauer, d. P.: The ERA- Interim reanalysis: Configuration and
616 performance of the data assimilation system, *Quarterly Journal of the royal meteorological society*,
617 137, 553-597, 2011.

618 Dorigo, W., Wagner, W., Albergel, C., Albrecht, F., Balsamo, G., Brocca, L., Chung, D., Ertl, M.,
619 Forkel, M., and Gruber, A.: ESA CCI Soil Moisture for improved Earth system understanding:
620 State-of-the art and future directions, *Remote Sensing of Environment*, 203, 185-215, 2017.

621 Dudhia, J.: Numerical study of convection observed during the winter monsoon experiment using
622 a mesoscale two-dimensional model, *Journal of the Atmospheric Sciences*, 46, 3077-3107, 1989.

623 Ek, M., Mitchell, K., Lin, Y., Rogers, E., Grunmann, P., Koren, V., Gayno, G., and Tarpley, J.:
624 Implementation of Noah land surface model advances in the National Centers for Environmental
625 Prediction operational mesoscale Eta model, *Journal of Geophysical Research: Atmospheres*, 108,
626 2003.

627 Fawcett, T.: An introduction to ROC analysis, *Pattern recognition letters*, 27, 861-874, 2006.

628 Gao, Q., Zribi, M., Escorihuela, M., and Baghdadi, N. J. S.: Synergetic use of Sentinel-1 and
629 Sentinel-2 data for soil moisture mapping at 100 m resolution, 17, 1966, 2017.

630 Gariano, S. L., Brunetti, M. T., Iovine, G., Melillo, M., Peruccacci, S., Terranova, O., Vennari, C.,
631 and Guzzetti, F.: Calibration and validation of rainfall thresholds for shallow landslide forecasting
632 in Sicily, southern Italy, *Geomorphology*, 228, 653-665, 2015.

633 Geudtner, D., Torres, R., Snoeij, P., Davidson, M., and Rommen, B.: Sentinel-1 system capabilities
634 and applications, 2014 IEEE Geoscience and Remote Sensing Symposium, 2014, 1457-1460,

635 Gilliland, E. K., and Rowe, C. M.: A comparison of cumulus parameterization schemes in the
636 WRF model, *Proceedings of the 87th AMS Annual Meeting & 21th Conference on Hydrology*,
637 2007,

638 Glade, T., Crozier, M., and Smith, P.: Applying probability determination to refine landslide-
639 triggering rainfall thresholds using an empirical “Antecedent Daily Rainfall Model”, *Pure and*
640 *Applied Geophysics*, 157, 1059-1079, 2000.

641 Goswami, S., Chakraborty, S., Ghosh, S., Chakrabarti, A., and Chakraborty, B. J. A. S. E. J.: A
642 review on application of data mining techniques to combat natural disasters, 9, 365-378, 2018.

643 Greve, P., Warrach-Sagi, K., and Wulfmeyer, V.: Evaluating soil water content in a WRF-Noah
644 downscaling experiment, *Journal of Applied Meteorology and Climatology*, 52, 2312-2327, 2013.

645 Hawke, R., and McConchie, J.: In situ measurement of soil moisture and pore-water pressures in
646 an ‘incipient’ landslide: Lake Tutira, New Zealand, *Journal of environmental management*, 92,
647 266-274, 2011.

648 Hong, S.-Y., Noh, Y., and Dudhia, J.: A new vertical diffusion package with an explicit treatment
649 of entrainment processes, *Monthly Weather Review*, 134, 2318-2341, 2006.

650 Hosmer, D., and Lemeshow, S.: *Applied logistic regression*. 1989, New York: Johns Wiley & Sons,
651 1989.

652 Jiménez, P. A., Dudhia, J., González-Rouco, J. F., Navarro, J., Montávez, J. P., and García-
653 Bustamante, E.: A revised scheme for the WRF surface layer formulation, *Monthly Weather*
654 *Review*, 140, 898-918, 2012.

655 Jordan, R.: A one-dimensional temperature model for a snow cover: Technical documentation for
656 SNTHERM. 89, Cold Regions Research and Engineering Laboratory, 1991.

657 Kain, J. S.: The Kain-Fritsch convective parameterization: An update, *Journal of Applied*
658 *Meteorology*, 43, [http://dx.doi.org/10.1175/1520-0450\(2004\)043<0170:TKCPAU>2.0.CO;2](http://dx.doi.org/10.1175/1520-0450(2004)043<0170:TKCPAU>2.0.CO;2),
659 2004.

660 Klose, M., Highland, L., Damm, B., and Terhorst, B.: Estimation of Direct Landslide Costs in
661 Industrialized Countries: Challenges, Concepts, and Case Study, in: *Landslide Science for a Safer*
662 *Geoenvironment*, World Landslide Forum 3, China (Beijing), 2014, 661-667,

663 Lagomarsino, D., Segoni, S., Fanti, R., and Catani, F. J. L.: Updating and tuning a regional-scale
664 landslide early warning system, 10, 91-97, 2013.

665 Lagomarsino, D., Segoni, S., Rosi, A., Rossi, G., Battistini, A., Catani, F., Casagli, N. J. N. H.,
666 and Sciences, E. S.: Quantitative comparison between two different methodologies to define
667 rainfall thresholds for landslide forecasting, 15, 2413-2423, 2015.

668 Lawrence, D. M., and Slater, A. G.: Incorporating organic soil into a global climate model, *Climate*
669 *Dynamics*, 30, 145-160, 2008.

670 Lawrence, D. M., Oleson, K. W., Flanner, M. G., Thornton, P. E., Swenson, S. C., Lawrence, P.
671 J., Zeng, X., Yang, Z. L., Levis, S., and Sakaguchi, K.: Parameterization improvements and
672 functional and structural advances in version 4 of the Community Land Model, *Journal of*
673 *Advances in Modeling Earth Systems*, 3, 27, 2011.

674 Lawrence, D. M., Oleson, K. W., Flanner, M. G., Fletcher, C. G., Lawrence, P. J., Levis, S.,
675 Swenson, S. C., and Bonan, G. B.: The CCSM4 land simulation, 1850–2005: Assessment of
676 surface climate and new capabilities, *Journal of Climate*, 25, 2240-2260, 2012.

677 Leung, L. R., and Qian, Y.: Atmospheric rivers induced heavy precipitation and flooding in the
678 western US simulated by the WRF regional climate model, *Geophysical research letters*, 36, 2009.

679 Liang, X., Xie, Z., and Huang, M.: A new parameterization for surface and groundwater
680 interactions and its impact on water budgets with the variable infiltration capacity (VIC) land
681 surface model, *Journal of Geophysical Research: Atmospheres*, 108, 2003.

682 Maheu, A., Anctil, F., Gaborit, É., Fortin, V., Nadeau, D. F., and Therrien, R.: A field evaluation
683 of soil moisture modelling with the Soil, Vegetation, and Snow (SVS) land surface model using
684 evapotranspiration observations as forcing data, *Journal of Hydrology*, 558, 532-545, 2018.

685 Martelloni, G., Segoni, S., Fanti, R., and Catani, F. J. L.: Rainfall thresholds for the forecasting of
686 landslide occurrence at regional scale, 9, 485-495, 2012.

687 Mlawer, E. J., Taubman, S. J., Brown, P. D., Iacono, M. J., and Clough, S. A.: Radiative transfer
688 for inhomogeneous atmospheres: RRTM, a validated correlated- k model for the longwave,
689 *Journal of Geophysical Research: Atmospheres*, 102, 16663-16682, 1997.

690 Weather research and forecasting model, 2018.

691 Nichol, J., and Wong, M. J. I. j. o. r. s.: Satellite remote sensing for detailed landslide inventories
692 using change detection and image fusion, 26, 1913-1926, 2005.

693 Niu, G. Y., Yang, Z. L., Dickinson, R. E., and Gulden, L. E.: A simple TOPMODEL- based runoff
694 parameterization (SIMTOP) for use in global climate models, *Journal of Geophysical Research:*
695 *Atmospheres*, 110, 2005.

696 Niu, G. Y., Yang, Z. L., Dickinson, R. E., Gulden, L. E., and Su, H.: Development of a simple
697 groundwater model for use in climate models and evaluation with Gravity Recovery and Climate
698 Experiment data, *Journal of Geophysical Research: Atmospheres*, 112, 2007.

699 Niu, G. Y., Yang, Z. L., Mitchell, K. E., Chen, F., Ek, M. B., Barlage, M., Kumar, A., Manning,
700 K., Niyogi, D., and Rosero, E.: The community Noah land surface model with

701 multiparameterization options (Noah- MP): 1. Model description and evaluation with local- scale
702 measurements, *Journal of Geophysical Research: Atmospheres*, 116, 2011.

703 Oleson, K., Niu, G. Y., Yang, Z. L., Lawrence, D., Thornton, P., Lawrence, P., Stöckli, R.,
704 Dickinson, R., Bonan, G., and Levis, S.: Improvements to the Community Land Model and their
705 impact on the hydrological cycle, *Journal of Geophysical Research: Biogeosciences (2005–2012)*,
706 113, 2008.

707 Oleson, K. W., Lawrence, D. M., Gordon, B., Flanner, M. G., Kluzek, E., Peter, J., Levis, S.,
708 Swenson, S. C., Thornton, E., and Feddema, J.: Technical description of version 4.0 of the
709 Community Land Model (CLM), 2010.

710 Paloscia, S., Pettinato, S., Santi, E., Notarnicola, C., Pasolli, L., and Reppucci, A. J. R. S. o. E.:
711 Soil moisture mapping using Sentinel-1 images: Algorithm and preliminary validation, 134, 234-
712 248, 2013.

713 Pistocchi, A., Bouraoui, F., and Bittelli, M.: A simplified parameterization of the monthly topsoil
714 water budget, *Water Resources Research*, 44, 2008.

715 Ponziani, F., Pandolfo, C., Stelluti, M., Berni, N., Brocca, L., and Moramarco, T. J. L.: Assessment
716 of rainfall thresholds and soil moisture modeling for operational hydrogeological risk prevention
717 in the Umbria region (central Italy), 9, 229-237, 2012.

718 Posner, A. J., and Georgakakos, K. P.: Soil moisture and precipitation thresholds for real-time
719 landslide prediction in El Salvador, *Landslides*, 12, 1179-1196, 2015.

720 Rossi, M., Witt, A., Guzzetti, F., Malamud, B. D., Peruccacci, S. J. E. S. P., and Landforms:
721 Analysis of historical landslide time series in the Emilia- Romagna region, northern Italy, 35,
722 1123-1137, 2010.

723 Segoni, S., Lagomarsino, D., Fanti, R., Moretti, S., and Casagli, N.: Integration of rainfall
724 thresholds and susceptibility maps in the Emilia Romagna (Italy) regional-scale landslide warning
725 system, *Landslides*, 12, 773-785, 2015.

726 Segoni, S., Rosi, A., Fanti, R., Gallucci, A., Monni, A., and Casagli, N. J. W.: A Regional-Scale
727 Landslide Warning System Based on 20 Years of Operational Experience, 10, 1297, 2018a.

728 Segoni, S., Rosi, A., Lagomarsino, D., Fanti, R., and Casagli, N.: Brief communication: Using
729 averaged soil moisture estimates to improve the performances of a regional-scale landslide early
730 warning system, *Natural Hazards and Earth System Sciences*, 18, 807-812, 2018b.

731 Skamarock, W., Klemp, J., Dudhia, J., Gill, D., Barker, D., Duda, M., Huang, X., Wang, W., and
732 Powers, J.: A description of the advanced research WRF Version 3, NCAR technical note,
733 Mesoscale and Microscale Meteorology Division, National Center for Atmospheric Research,
734 Boulder, Colorado, USA, 2008.

735 Skamarock, W. C., Klemp, J. B., Dudhia, J., Gill, D. O., Barker, D. M., Wang, W., and Powers, J.
736 G.: A description of the advanced research WRF version 2, National Center For Atmospheric
737 Research Boulder Co Mesoscale and Microscale Meteorology Div, 2005.

738 Srivastava, P. K., Han, D., Rico-Ramirez, M. A., Al-Shrafany, D., and Islam, T.: Data fusion
739 techniques for improving soil moisture deficit using SMOS satellite and WRF-NOAH land surface
740 model, *Water resources management*, 27, 5069-5087, 2013a.

741 Srivastava, P. K., Han, D., Rico Ramirez, M. A., and Islam, T.: Comparative assessment of
742 evapotranspiration derived from NCEP and ECMWF global datasets through Weather Research
743 and Forecasting model, *Atmospheric Science Letters*, 14, 118-125, 2013b.

744 Srivastava, P. K., Han, D., Rico-Ramirez, M. A., O'Neill, P., Islam, T., Gupta, M., and Dai, Q.:
745 Performance evaluation of WRF-Noah Land surface model estimated soil moisture for
746 hydrological application: Synergistic evaluation using SMOS retrieved soil moisture, *Journal of*
747 *Hydrology*, 529, 200-212, 2015.

748 Stéfanon, M., Drobinski, P., D'Andrea, F., Lebeaupin-Brossier, C., and Bastin, S.: Soil moisture-
749 temperature feedbacks at meso-scale during summer heat waves over Western Europe, *Climate*
750 *dynamics*, 42, 1309-1324, 2014.

751 Temimi, M., Leconte, R., Chaouch, N., Sukumal, P., Khanbilvardi, R., and Brissette, F.: A
752 combination of remote sensing data and topographic attributes for the spatial and temporal
753 monitoring of soil wetness, *Journal of Hydrology*, 388, 28-40, 2010.

754 Thompson, G., Field, P. R., Rasmussen, R. M., and Hall, W. D.: Explicit forecasts of winter
755 precipitation using an improved bulk microphysics scheme. Part II: Implementation of a new snow
756 parameterization, *Monthly Weather Review*, 136, 5095-5115, 2008.

757 Tsai, T.-L., and Chen, H.-F.: Effects of degree of saturation on shallow landslides triggered by
758 rainfall, *Environmental Earth Sciences*, 59, 1285-1295, 2010.

759 Valenzuela, P., Domínguez-Cuesta, M. J., García, M. A. M., and Jiménez-Sánchez, M.: Rainfall
760 thresholds for the triggering of landslides considering previous soil moisture conditions (Asturias,
761 NW Spain), *Landslides*, 15, 273-282, 2018.

762 Van Den Broeke, M. S., Kalin, A., Alavez, J. A. T., Oglesby, R., Hu, Q. J. T., and climatology, a.:
763 A warm-season comparison of WRF coupled to the CLM4. 0, Noah-MP, and Bucket hydrology
764 land surface schemes over the central USA, 134, 801-816, 2018.

765 Wei, J., Dirmeyer, P. A., Guo, Z., Zhang, L., and Misra, V.: How much do different land models
766 matter for climate simulation? Part I: Climatology and variability, *Journal of Climate*, 23, 3120-
767 3134, 2010.

768 Wharton, S., Simpson, M., Osuna, J., Newman, J., and Biraud, S.: Assessment of Land Surface
769 Model Performance in WRF for Simulating Wind at Heights Relevant to the Wind Energy
770 Community, Lawrence Livermore National Lab (LLNL), Livermore, CA (United States), 2013.

771 Wilks, D.: *Statistical Methods in the Atmospheric Sciences*, 3rd ed., Academic Press, 2011.

772 Yang, Z. L., Niu, G. Y., Mitchell, K. E., Chen, F., Ek, M. B., Barlage, M., Longuevergne, L.,
773 Manning, K., Niyogi, D., and Tewari, M.: The community Noah land surface model with
774 multiparameterization options (Noah- MP): 2. Evaluation over global river basins, *Journal of*
775 *Geophysical Research: Atmospheres*, 116, 2011.

776 Zaidi, S. M., and Gisen, J. I. A.: Evaluation of Weather Research and Forecasting (WRF)
777 Microphysics single moment class-3 and class-6 in Precipitation Forecast, MATEC Web of
778 Conferences, 2018, 03007,

779 Zaitchik, B. F., Santanello, J. A., Kumar, S. V., and Peters-Lidard, C. D.: Representation of soil
780 moisture feedbacks during drought in NASA unified WRF (NU-WRF), *Journal of*
781 *Hydrometeorology*, 14, 360-367, 2013.

782 Zeng, X., and Decker, M.: Improving the numerical solution of soil moisture-based Richards
783 equation for land models with a deep or shallow water table, *Journal of Hydrometeorology*, 10,
784 308-319, 2009.

785 Zhao, B., Dai, Q., Han, D., Dai, H., Mao, J., and Zhuo, L.: Antecedent wetness and rainfall
786 information in landslide threshold definition, *Hydrol. Earth Syst. Sci. Discuss.*, 2019, 1-26,
787 10.5194/hess-2019-150, 2019a.

788 Zhao, B., Dai, Q., Han, D., Dai, H., Mao, J., and Zhuo, L. J. J. o. H.: Probabilistic thresholds for
789 landslides warning by integrating soil moisture conditions with rainfall thresholds, 574, 276-287,
790 2019b.

791 Zhuo, L., Dai, Q., and Han, D.: Evaluation of SMOS soil moisture retrievals over the central United
792 States for hydro-meteorological application, *Physics and Chemistry of the Earth, Parts A/B/C*, 83,
793 146-155, 2015a.

794 Zhuo, L., Han, D., Dai, Q., Islam, T., and Srivastava, P. K.: Appraisal of NLDAS-2 multi-model
795 simulated soil moistures for hydrological modelling, *Water resources management*, 29, 3503-3517,
796 2015b.

797 Zhuo, L., Dai, Q., Han, D., Chen, N., Zhao, B., and Berti, M.: Evaluation of remotely sensed soil
798 moisture for landslide hazard assessment, *IEEE Journal of Selected Topics in Applied Earth
799 Observations and Remote Sensing*, 12, 162 - 173, 2019.

800

Table 1. Comparison of Noah, Noah-MP, and CLM4.

	Noah	Noah-MP	CLM4
Energy balance	Yes	Yes	Yes
Water balance	Yes	Yes	Yes
No. of soil layers	4	4	10
Depth of total soil column	2.0 m	2.0 m	3.802 m
Model soil layer thickness	0.1, 0.3, 0.6, 1.0 m	0.1, 0.3, 0.6, 1.0 m	0.018, 0.028, 0.045, 0.075, 0.124, 0.204, 0.336, 0.553, 0.913, 1.506 m
No. of vegetation layers	A single combined surface layer of vegetation and snow	Single layer	Single layer
Vegetation	Dominant vegetation type in one grid cell with prescribed LAI	Dominant vegetation type in one grid cell with dynamic LAI	Up to 10 vegetation types in one grid cell with prescribed LAI
No. of snow layers	A single combined surface layer of vegetation and snow	Up to three layers	Up to five layers

Table 2. WRF parameterizations used in this study.

	Settings/ Parameterizations	References
Map projection	Lambert	
Central point of domain	Latitude: 44.54; Longitude: 11.02	
Latitudinal grid length	5 km	
Longitudinal grid length	5 km	
Model output time step	Daily	
Nesting	Two-way	
Land surface model	Noah, Noah-MP, CLM	
Simulation period	1/1/2006 – 31/12/2015	
Spin-up period	1/1/2005 – 31/12/2005	
Microphysics	New Thompson	(Thompson et al., 2008)
Shortwave radiation	Dudhia scheme	(Dudhia, 1989)
Longwave radiation	Rapid Radiative Transfer Model	(Mlawer et al., 1997)
Surface layer	Revised MM5	(Jiménez et al., 2012; Chen and Dudhia, 2001)
Planetary boundary layer	Yonsei University method	(Hong et al., 2006)
Cumulus Parameterization	Kain-Fritsch (new Eta) scheme	(Kain, 2004)

Table 3. Statistical summary of the WRF performance in simulating soil moisture for different soil layers, based on comparison with the single point in-situ observations.

	<i>R</i>				<i>RMSE (m³/m³)</i>			
	0.10 m	0.25 m	0.70 m	1.50 m	0.1 m	0.25 m	0.70 m	1.50 m
Noah	0.728	0.645	0.660	0.430	0.123	0.125	0.141	0.055
Noah-MP	0.809	0.683	0.738	0.498	0.060	0.070	0.088	0.092
CLM	0.789	0.743	0.648	0.287	0.089	0.087	0.123	0.089

Table 4. Statistical summary of the WRF performance in simulating rainfall for the whole study region, based on comparison with the in-situ rainfall network.

	<i>R</i>			<i>RMSE (mm)</i>		
	Noah	Noah-MP	CLM4	Noah	Noah-MP	CLM4
Min	0.094	0.090	0.076	4.275	4.286	4.219
Max	0.779	0.798	0.801	19.814	19.178	19.476
Mean	0.425	0.426	0.421	7.772	7.719	7.943
0.25 percentile	0.147	0.130	0.154	4.579	4.297	4.438
0.50 percentile	0.189	0.153	0.210	4.951	4.909	4.910
0.75 percentile	0.192	0.183	0.211	5.006	4.970	5.010

Table 5. Rainfall events information.

Starting date			Ending date			Duration (days)	Rainfall intensity (mm/day)	Number of Landslide events
Year	Month	Day	Year	Month	Day			
2014	1	13	2014	1	24	12	20.50	2
2014	1	28	2014	2	14	18	13.61	0
2014	2	26	2014	3	6	9	13.35	0
2014	3	22	2014	3	27	6	11.08	0
2014	4	4	2014	4	5	2	18.98	0
2014	4	27	2014	5	4	8	12.13	0
2014	5	26	2014	6	3	9	5.05	0
2014	6	14	2014	6	16	3	18.29	0
2014	6	25	2014	6	30	6	11.39	0
2014	7	7	2014	7	14	8	7.84	0
2014	7	21	2014	7	30	10	15.35	0
2014	8	31	2014	9	5	6	5.67	0
2014	9	10	2014	9	12	3	11.84	0
2014	9	19	2014	9	20	2	23.04	0
2014	10	1	2014	10	1	1	14.51	0
2014	10	10	2014	10	17	8	13.01	0
2014	11	4	2014	11	18	15	18.28	0
2014	11	25	2014	12	7	13	7.58	0
2014	12	13	2014	12	16	4	6.24	0
2015	1	16	2015	1	17	2	14.87	0
2015	1	21	2015	1	23	3	7.13	0
2015	1	29	2015	2	10	13	9.98	0
2015	2	13	2015	2	17	5	6.62	1
2015	2	21	2015	2	26	6	11.84	4
2015	3	3	2015	3	7	5	11.69	1
2015	3	15	2015	3	17	3	9.00	0
2015	3	21	2015	3	27	7	12.09	2
2015	4	3	2015	4	5	3	16.62	0
2015	4	17	2015	4	18	2	6.99	0
2015	4	26	2015	4	29	4	11.23	0
2015	5	15	2015	5	16	2	8.83	0
2015	5	20	2015	5	27	8	10.58	1
2015	6	8	2015	6	11	4	6.47	0
2015	6	16	2015	6	19	4	13.44	0
2015	6	23	2015	6	24	2	6.07	0
2015	7	22	2015	7	25	4	6.05	0
2015	8	9	2015	8	10	2	24.69	0
2015	8	15	2015	8	19	5	10.69	0
2015	8	23	2015	8	24	2	7.88	0
2015	9	13	2015	9	14	2	24.66	1
2015	9	23	2015	9	24	2	7.50	0
2015	10	1	2015	10	7	7	13.73	0
2015	10	10	2015	10	19	10	9.40	0
2015	10	27	2015	10	29	3	20.33	0
2015	11	21	2015	11	25	5	13.78	1

Table 6. Results of Euclidean distances (d) between individual points and the optimal point for ROC analysis are listed. The best performance (i.e., lowest d) for each column (i.e., each soil layer of an LSM scheme) is highlighted. The optimal performance of all is highlighted in red.

<i>e.p.</i> (%)	Noah				Noah-MP				CLM4			
	10 cm	25 cm	70 cm	150 cm	10 cm	25 cm	70 cm	150 cm	10 cm	25 cm	70 cm	150 cm
1	0.942	0.971	0.962	0.947	0.857	0.937	0.897	0.963	0.942	0.939	0.978	0.975
2	0.906	0.945	0.963	0.923	0.854	0.912	0.883	0.959	0.923	0.922	0.959	0.952
3	0.889	0.924	0.961	0.915	0.849	0.855	0.838	0.952	0.870	0.874	0.940	0.947
4	0.884	0.898	0.946	0.914	0.838	0.814	0.829	0.924	0.831	0.843	0.925	0.947
5	0.860	0.875	0.924	0.896	0.820	0.793	0.812	0.908	0.791	0.822	0.915	0.921
6	0.835	0.854	0.910	0.874	0.803	0.785	0.800	0.905	0.770	0.817	0.911	0.909
7	0.827	0.861	0.902	0.858	0.777	0.767	0.791	0.889	0.753	0.801	0.902	0.900
8	0.816	0.849	0.889	0.851	0.745	0.765	0.782	0.876	0.745	0.785	0.902	0.910
9	0.790	0.827	0.878	0.834	0.706	0.732	0.766	0.871	0.742	0.777	0.864	0.904
10	0.762	0.811	0.863	0.825	0.672	0.702	0.747	0.862	0.738	0.767	0.835	0.887
15	0.615	0.741	0.839	0.763	0.560	0.629	0.716	0.835	0.702	0.700	0.729	0.790
20	0.485	0.627	0.779	0.652	0.515	0.571	0.624	0.774	0.570	0.602	0.594	0.650
25	0.432	0.544	0.728	0.512	0.403	0.465	0.574	0.736	0.509	0.522	0.471	0.509
30	0.437	0.495	0.643	0.451	0.369	0.375	0.544	0.679	0.475	0.477	0.447	0.469
35	0.392	0.446	0.592	0.436	0.390	0.404	0.411	0.498	0.441	0.435	0.428	0.430
40	0.500	0.407	0.531	0.416	0.439	0.385	0.382	0.436	0.406	0.405	0.398	0.410
50	0.552	0.425	0.404	0.411	0.489	0.417	0.416	0.429	0.437	0.435	0.408	0.437

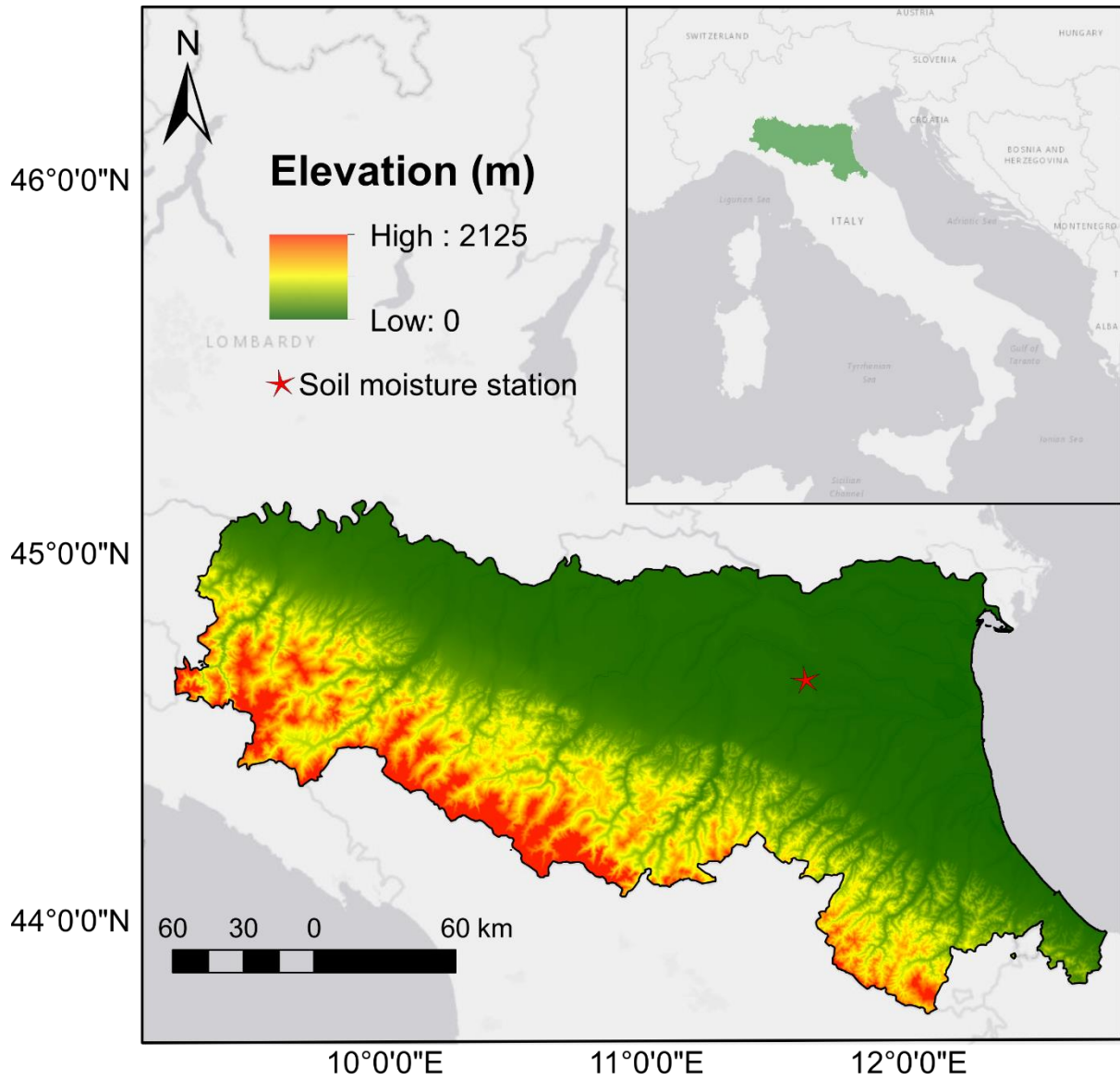


Figure 1. Location of the Emilia Romagna Region with elevation map and in-situ soil moisture station also shown.

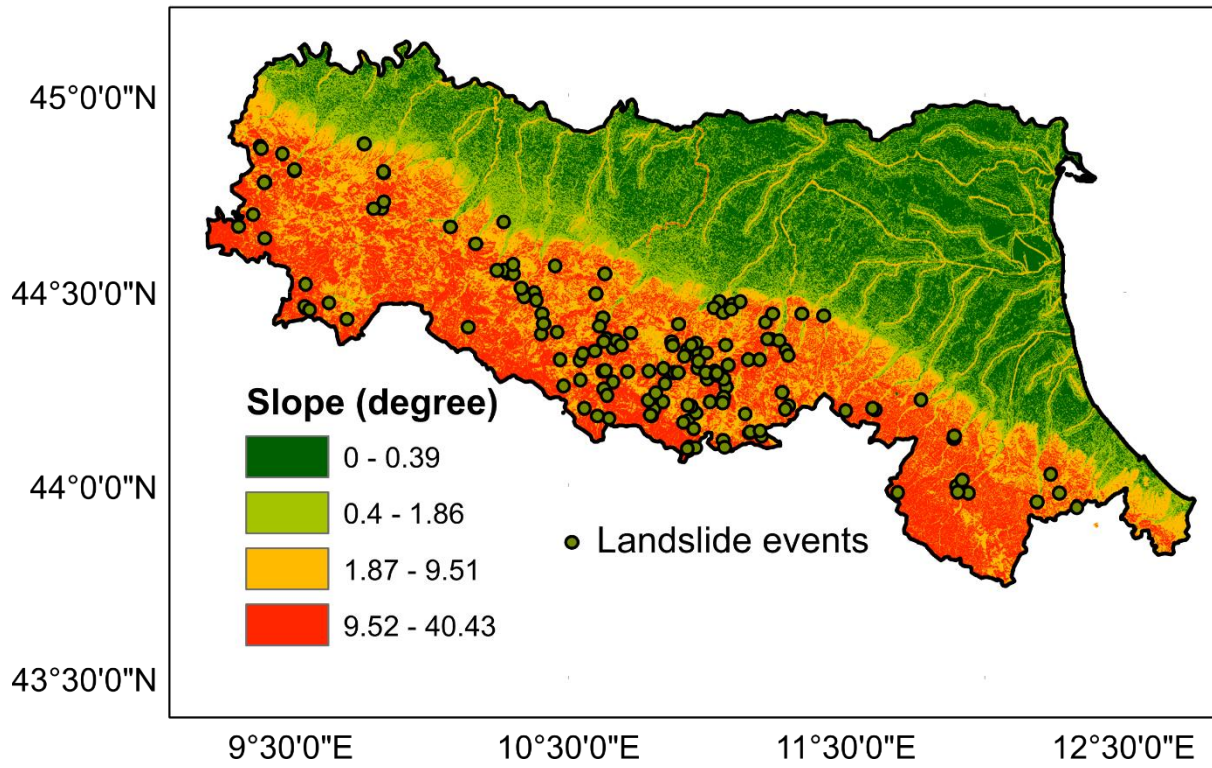


Figure 2. Landslide events with slope angle map.

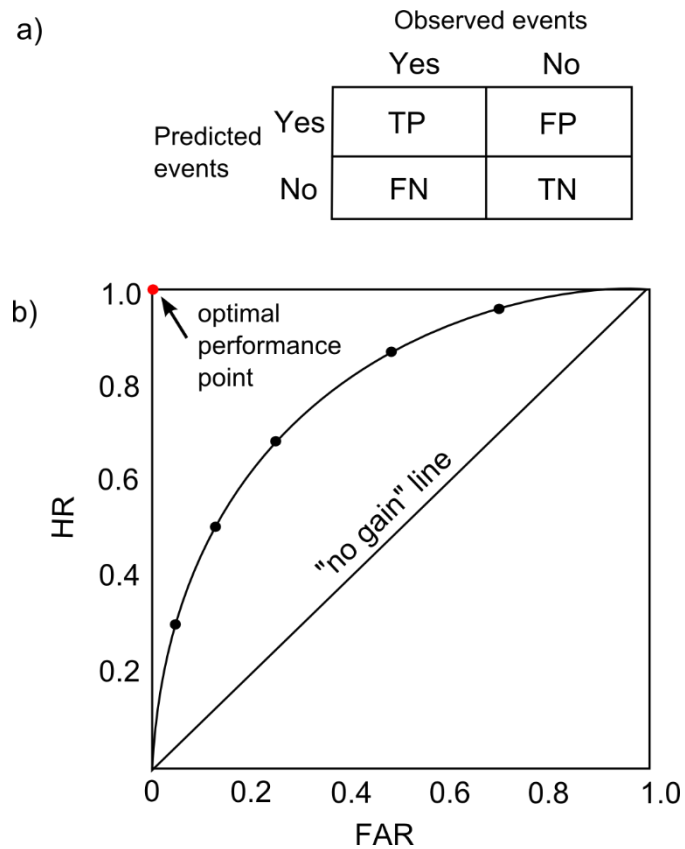


Figure 3. a) Contingency table illustrates the four possible outcomes of a binary classifier model: TP (True Positive), TN (True Negative), FP (False Positive), and FN (False Negative). b) ROC (Receiver Operating Characteristic) analysis with HR (Hitting Rate) against FAR (False Alarm Rate).

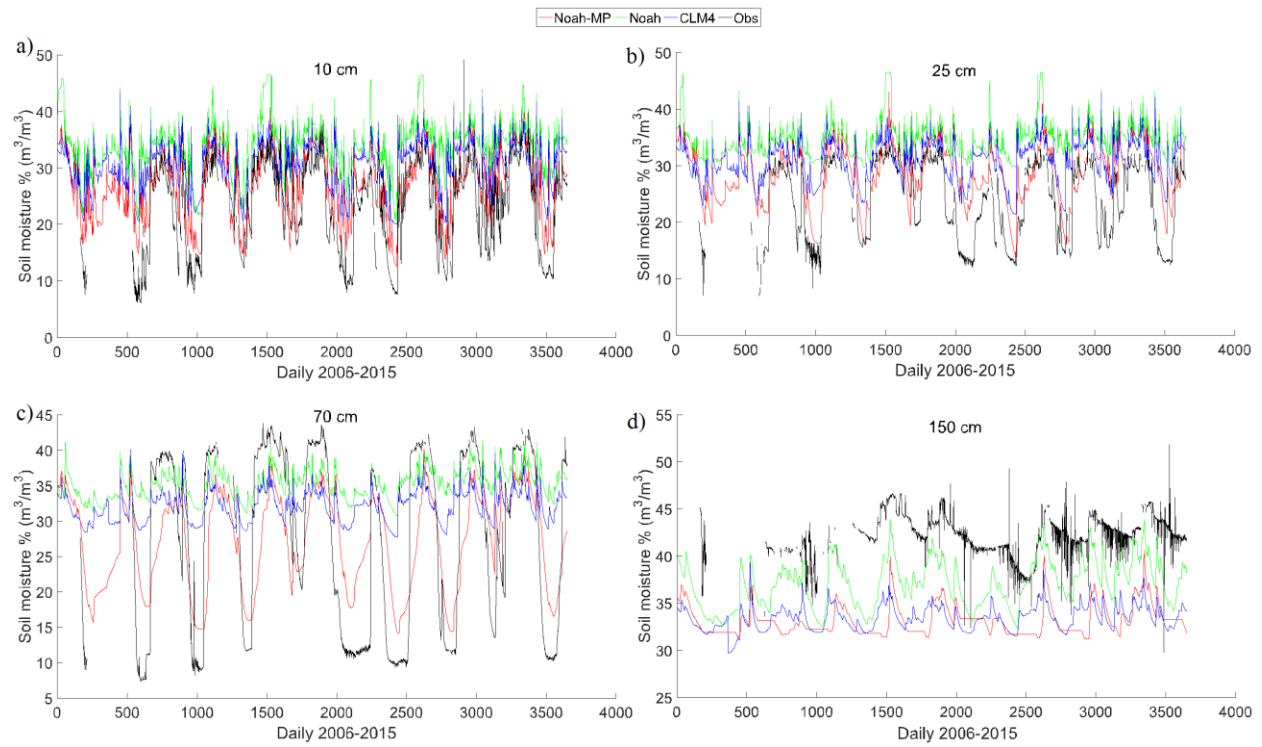


Figure 4. Soil moisture temporal variations of WRF simulations and in-situ observations for four soil layers at a) 10 cm; b) 25 cm; c) 70 cm; and d) 150 cm.

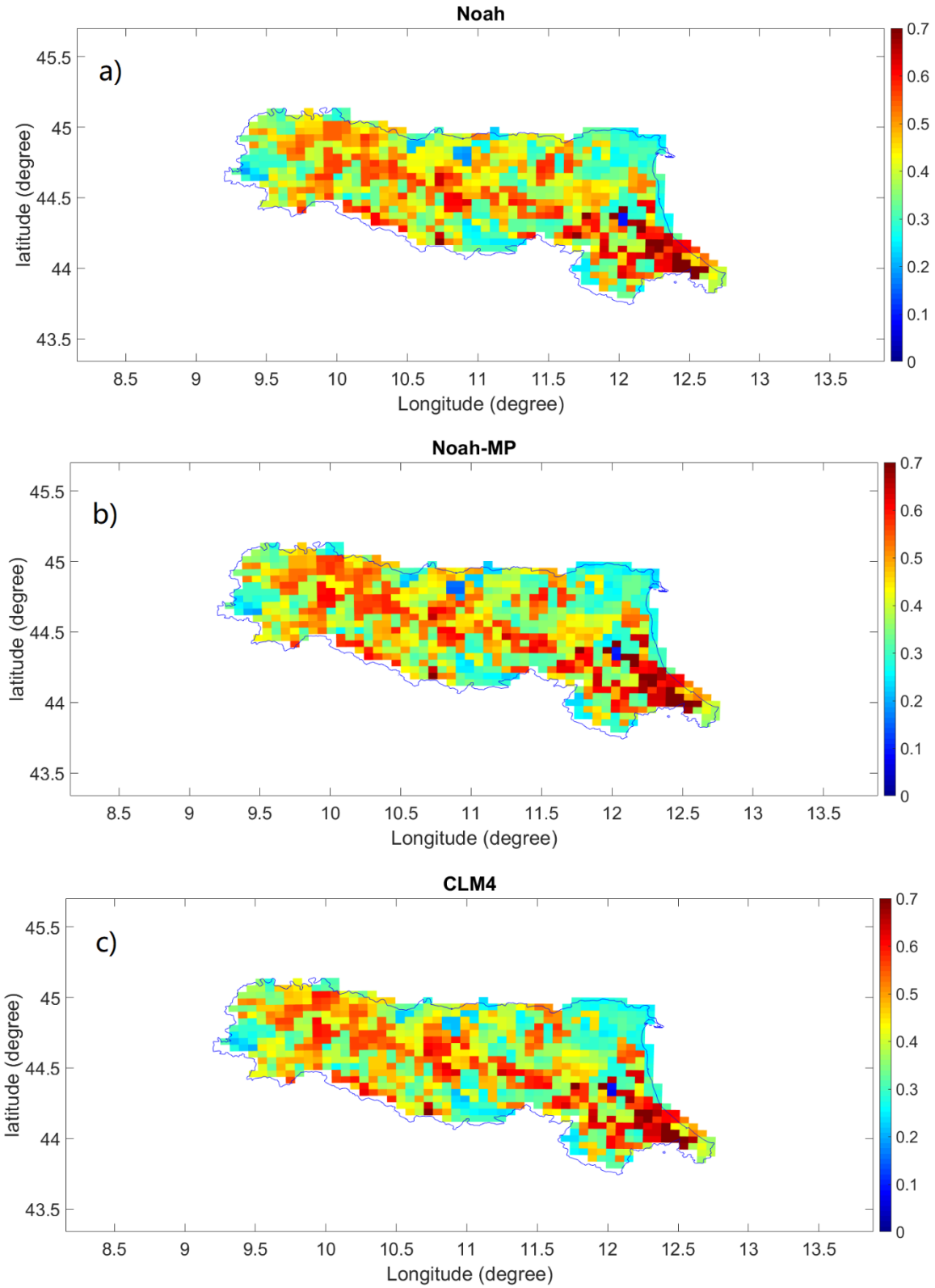


Figure 5. Rainfall evaluation: spatial distribution of the correlation coefficient R of a) Noah, b) Noah-MP and c) CLM4.

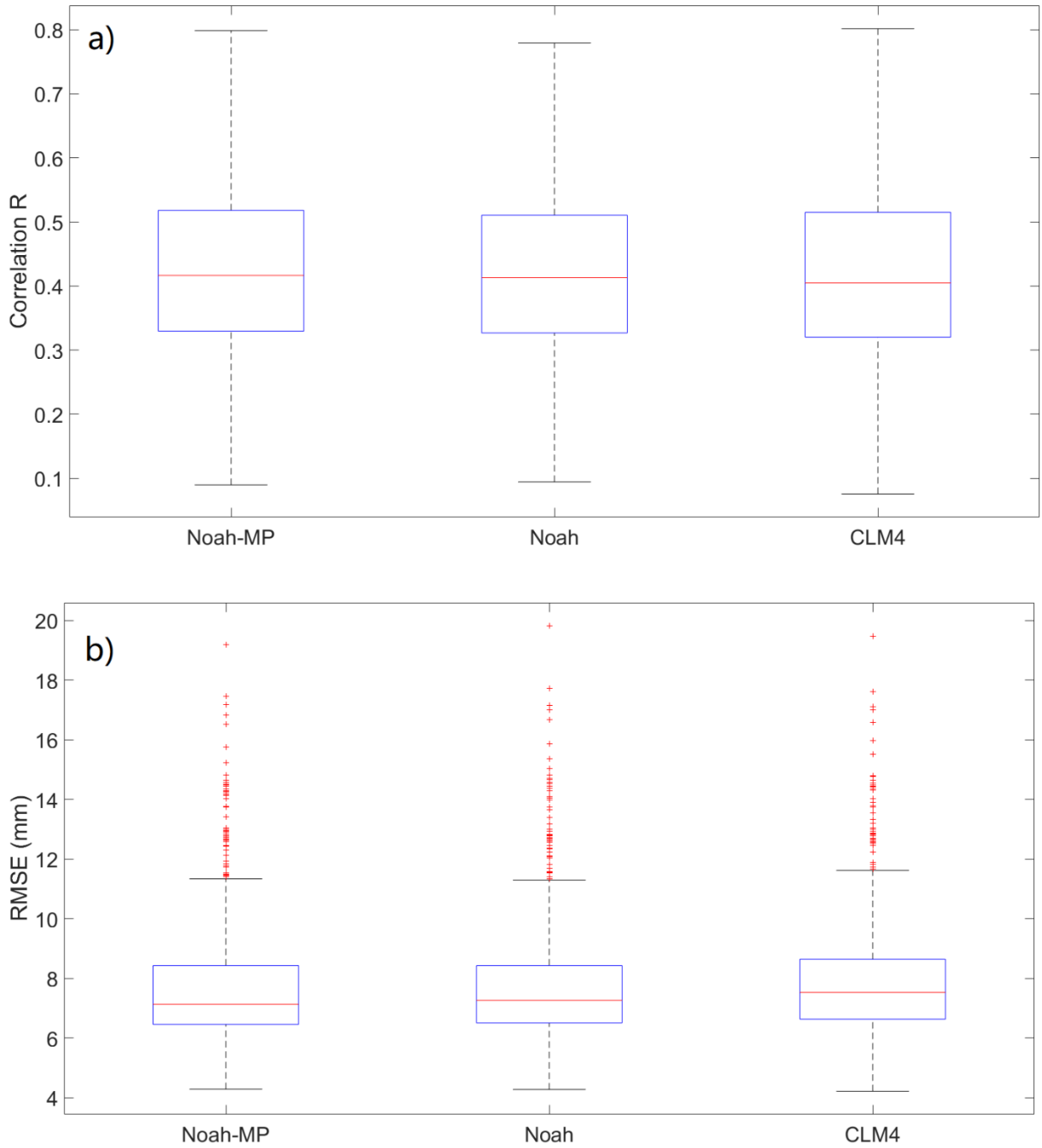


Figure 6. Boxplots of rainfall evaluation results of a) R and b) $RMSE$: minimum, maximum, 0.25, 0.50 and 0.75 percentiles, and outliers (red cross).

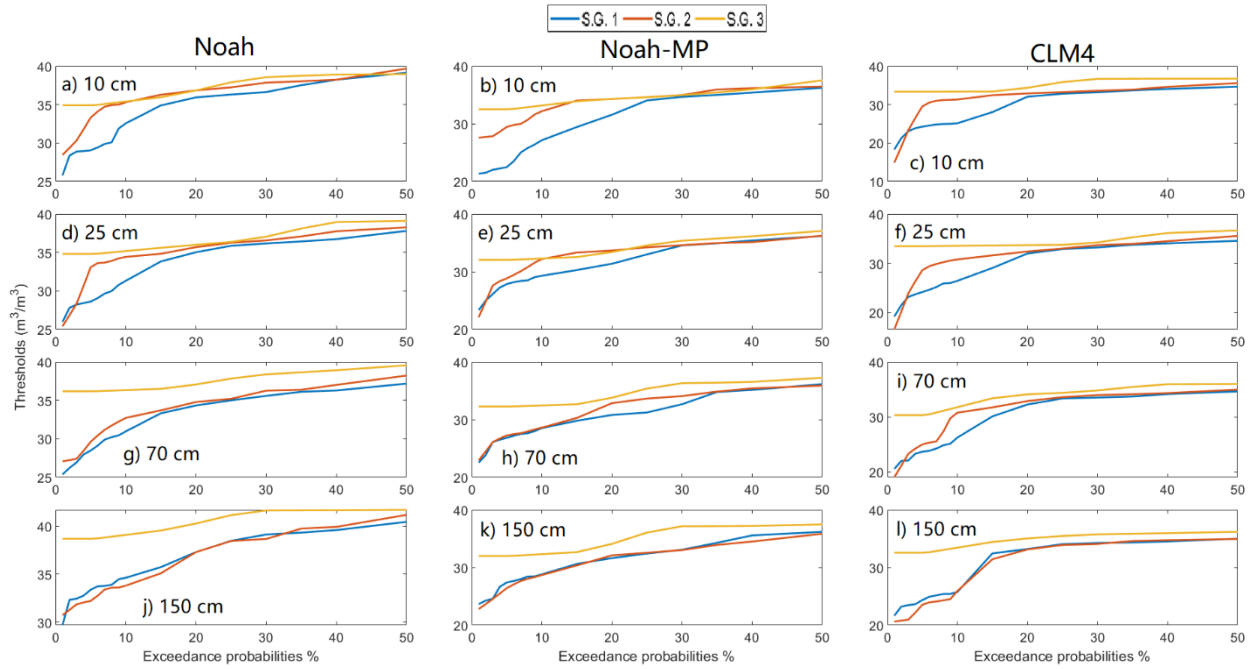


Figure 7. Threshold plots. For Noah (a, d, g, j), Noah-MP (b, e, h, k), and CLM4 (c, f, i, l) land surface schemes under three Slope angle Groups (S.G.) with S.G. 1 = 0.4-1.86°; S.G. 2 = 1.87-9.61°; S.G. 3 = 9.52-40.43°.

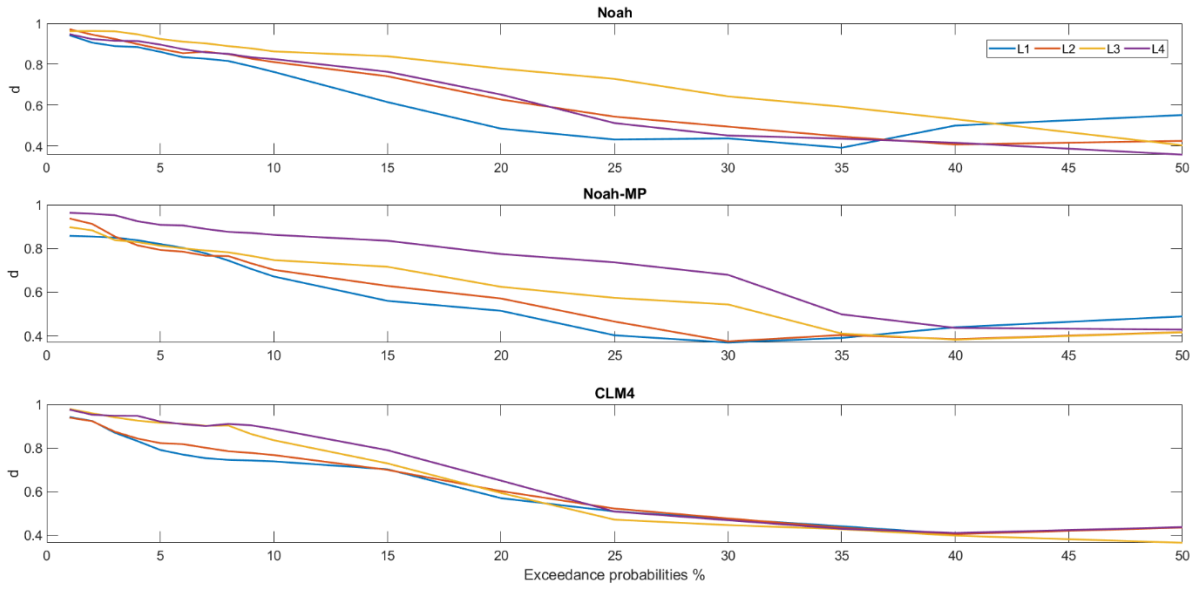


Figure 8. d-scores.

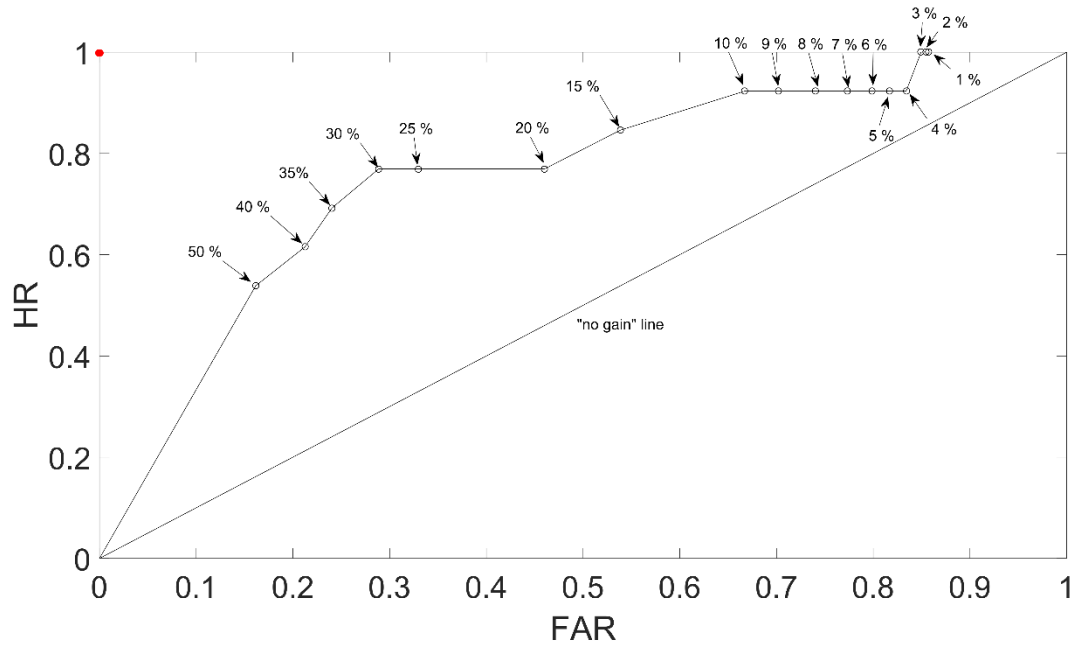


Figure 9. ROC curve for the calculated thresholds using different exceedance probability levels (for Noah-MP at the surface layer). The *no gain* line and the optimal performance point (the red point) are also presented.

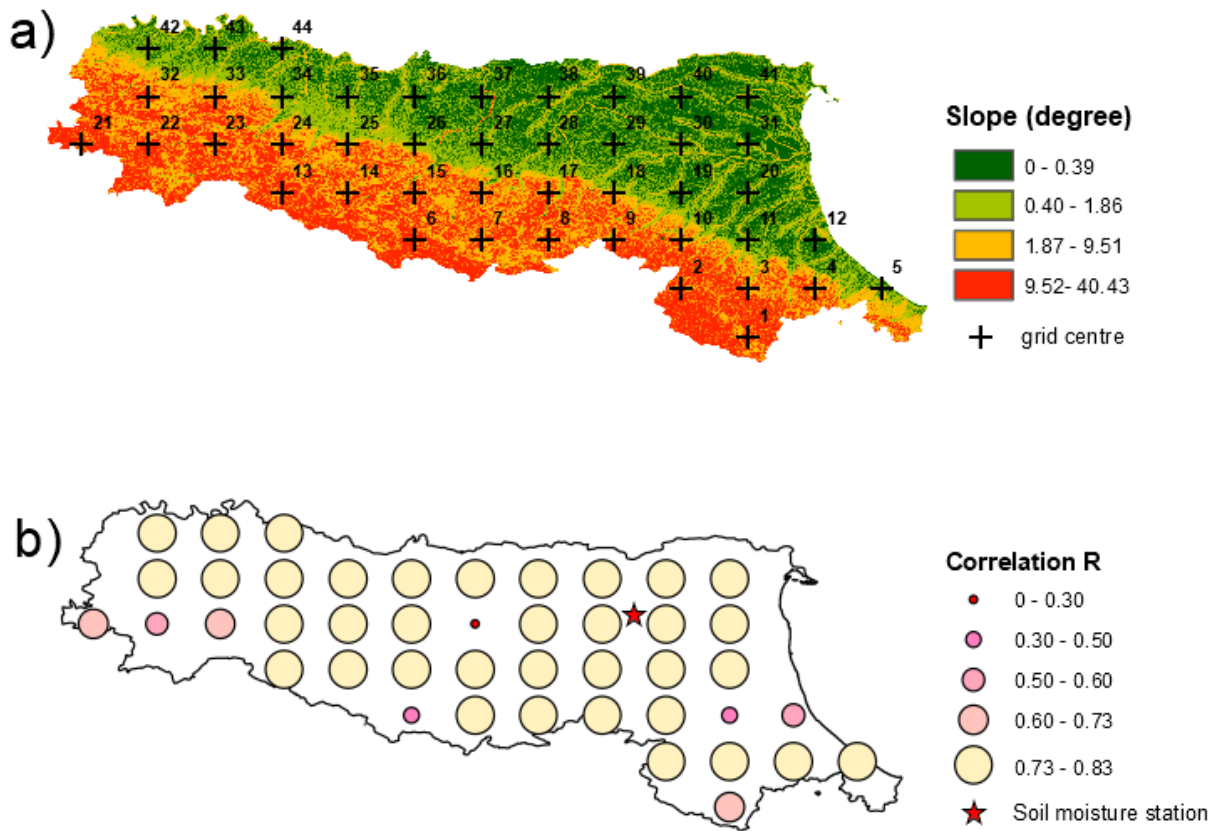


Figure 10. The cross-validation of spatially distributed WRF soil moisture against the in-situ soil moisture observation at the single point soil moisture sensor in plain area: a) grid numbers shown on the slope map, b) correlation spatial performance.

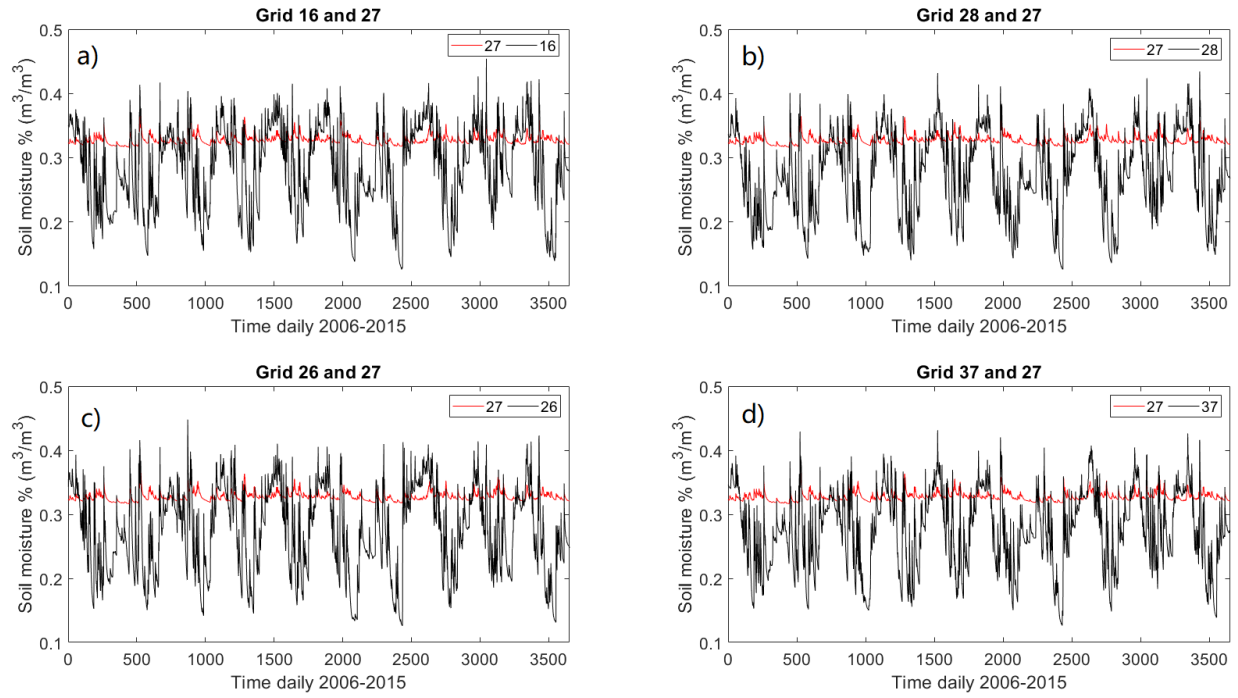


Figure 11. The soil moisture comparisons of Grid 27 with the adjacent grids (16, 28, 26, 37).